A new family of projection schemes for the incompressible Navier-Stokes equations with control of high-frequency damping

A. Lovrić*, Wulf G. Dettmer, Chennakesava Kadapa, Djordje Perić

Zienkiewicz Centre for Computational Engineering, College of Engineering, Swansea University, Fabian Way, Swansea SA1 8EN, Wales, UK

Abstract

A simple spatially discrete model problem consisting of mass points and dash-pots is presented which allows for the assessment of the properties of different projection schemes for the solution of the incompressible Navier-Stokes equations. In particular, the temporal accuracy, the stability and the numerical damping are investigated. The present study suggests that it is not possible to formulate a second order accurate projection/pressure-correction scheme which possesses any high-frequency damping. Motivated by this observation two new families of projection schemes are proposed which are developed from the generalised midpoint rule and from the generalised-α method, respectively, and offer control over high-frequency damping. Both schemes are investigated in detail on the basis of the model problem and subsequently implemented in the context of a finite element formulation for the incompressible Navier-Stokes equations. Comprehensive numerical studies of the flow in a lid-driven cavity and the flow around a cylinder are presented. The observations made are in agreement with the conclusions drawn from the model problem.

Keywords: Incompressible Navier-Stokes equations; Fractional step method; Projection method; Finite element method; Generalised-alpha method

1. Introduction

In the simulation of incompressible fluid flow, one of the main challenges is posed by the coupling of the velocity and pressure fields through the incompressibility constraint. This has motivated the development of fractional step or splitting methods. These methods are based on the decoupling of the velocity-pressure system by splitting it into a sequence of "fractional" or "segregated" solution steps. Although the general idea remains the same, this splitting has been formulated in a number of ways over the years; often in the form of projection methods [1, 2], pressure or velocity correction methods [3, 4, 5], consistent splitting methods [6], viscosity splitting methods [7] or characteristic-based split (CBS) methods [8], to name just a few. Arguably the most widely used fractional step methods for incompressible fluid flow are the original projection schemes proposed independently by Chorin [1] and Temam [2, 9] in the 1960's. In short, these projection methods are based on an orthogonal projection onto a subspace of solenoidal vector fields, see [2] for a thorough explanation. The basic idea is to acquire an intermediate velocity field (Step 1) by solving the momentum equation without the pressure gradient, i.e. considering only viscous, inertia and convection terms, and subsequently computing the pressure and divergence-free end-of-step velocity (Step 2). The appealing benefits of this approach consist in smaller system matrices, dimensionally uniform solution and right hand side vectors and, importantly, the fact that the pressure is obtained efficiently in Step 2 from solving the Poisson equation. The drawbacks of such strategies include additional complexity in the application of the boundary conditions and most of all the introduction of a so-called splitting error, which brings about a relative loss of temporal accuracy compared to a respective

*Corresponding author.
Email address: alexlovric@gmail.com (A. Lovrić)

coupled approach. Due to their semi-explicit nature, it is crucial that temporal stability and accuracy are in the focus of all development in the area of the fractional step solution schemes.

As mentioned above, in the classical projection methods by Chorin and Temam, the intermediate velocity is computed independently of the pressure. It is well-understood that this restricts these methods to first order accuracy in time. If, in the first step, the pressure is approximated by the solution from the previous time step, then a pressure increment can be computed in the second step and an overall second order accurate scheme can be formulated. This approach is typically known as the "incremental projection" or "pressure correction" method and was first considered in, for instance, [3, 4]. It is clear that the accuracy of the pressure extrapolation used in the first step must be increased in order to formulate a more accurate methodology. It is noted that, despite these efforts, the first order accurate schemes are still widely used. The analysis of the properties of the different schemes is not trivial and is an active area of research, see for instance [10, 11, 12, 13]. The present work has multiple objectives:

1. Presentation of a discrete model problem consisting of point masses and dash-pots which allows for detailed insight into the properties of projection schemes and is a useful tool for new development;
2. Discussion of high-frequency damping of projection schemes;
3. Presentation of two new families of projection schemes based on the generalised midpoint rule and the generalised-α method [14].

Prior to the further explanation of the objectives, it is pointed out that the work presented in this article is relevant for projection methods based on the finite volume as well as finite element formulations, even though Sections 3 and 4 are set in the context of the finite element method.

Objective 1 is motivated by the successful recent employment of the basic model problems in the area of the partitioned schemes for fluid-structure interaction. Here, the analyses of appropriate spatially discrete model problems has allowed for in-depth insight into temporal and added mass related instabilities [15, 16, 17] and is increasingly used for new method development [18, 19]. The investigation undertaken in the context of Objective 2 led to the observation that it is impossible to formulate a projection scheme for the model problem which is second order accurate and possesses high-frequency damping. This is an important finding which, to the best of our knowledge, has not been reported elsewhere and which may explain why second order accurate projection schemes have generally not replaced first order schemes. Objective 3 is the attempt to formulate a methodology which is more accurate than basic backward Euler based projection schemes, but offers some high-frequency damping.

The beneficial role of high-frequency damping in incremental numerical solution schemes for partial differential equations in time and space is well-known: The numerical analyst chooses the spatial and temporal discretisation suitable for the length and time scales which are of interest and represent the main system response. Hence, a robust methodology requires high-frequency damping to damp out the effect of the unresolved scales. In particular, high-frequency damping allows for a larger degree of independence between the spatial and temporal resolutions, i.e. a larger range of Courant numbers. In the context of the monolithic solution schemes for computational fluid dynamics, the generalised-α method, which is unconditionally stable, second order accurate and offers control over high-frequency damping, has therefore become very popular, see for instance [20, 21, 22, 23]. It was proposed in [14] and is related to its counterpart formulated earlier for solid dynamics in [24] (see also [25]). In the present work, a projection scheme is formulated based on the generalised-α method. It is shown clearly how the proposed methodology is related to the backward differencing schemes which are commonly employed for projection schemes.

A discussion of projection schemes generally also comments on the issue of spurious pressure oscillations. This is discussed briefly in Section 3.3. Another aspect which has been addressed in a number of publications is the occurrence of undesired effects due to non-physical artificial boundary conditions along Dirichlet boundaries [26, 27]. An extensive study of the "rotational forms" which remove such effects can be found in [11]. In [28] a corresponding formulation has been used in the context of fluid-structure interaction. Since, in the examples presented in Section 4, no evidence of non-physical boundary layers has been detected even for large time steps, the issue is not considered in this work. The proposed formulations can, however, also be applied to projection schemes which include the rotational forms.

The remainder of this work is structured as follows: In Section 2, the model problem is presented, the new projection schemes are proposed and applied to the model problem. The responses of the schemes and the spectral radii of the amplification matrices are studied in detail. In Section 3, the projection methods are formulated for the incompressible Navier-Stokes equations using finite elements. Numerical examples are presented in Section 4, before the conclusions are drawn in Section 5.

Throughout this article, the terms "monolithic" or "coupled" refer to solution schemes based on the simultaneous computation of velocities and pressures.

2. Analysis of projection schemes

2.1. 1D model problem with analytical solution

The model problem consists of a 1D mass-dashpot system with three degrees of freedom as shown in Figure 1. The motion of the masses are subject to the physical constraint,

$$\xi_1 u_1 + \xi_2 u_2 + \xi_3 u_3 = 0 \tag{2.1}$$

where ξ_1, ξ_2 and ξ_3 are scalar factors, and the velocities of the point masses are denoted by, respectively, u_1, u_2 and u_3. All point masses are equal. This choice does not imply a loss of generality, but allows for a clearer presentation which is more aligned with the formulation for the incompressible Navier-Stokes equations in Section 3. The constraint (2.1) is imposed on the system by employing a Lagrange multiplier. A thorough description of this methodology is given in Joosten *et al.* [17].

Thus, the governing equations read

$$\dot{\boldsymbol{u}} + \mathbf{C}\boldsymbol{u} + \mathbf{b}\lambda = \mathbf{0} \tag{2.2a}$$

$$\mathbf{b} \cdot \boldsymbol{u} = 0 \tag{2.2b}$$

where $\dot{\boldsymbol{u}} = \{\dot{u}_1, \dot{u}_2, \dot{u}_3\}^T$ and $\boldsymbol{u} = \{u_1, u_2, u_3\}^T$ are the accelerations and velocities of the point masses respectively and λ is the Lagrange multiplier. The matrix $\mathbf{C}$ and the vector $\mathbf{b}$ are

$$\mathbf{C} = \frac{1}{m}\begin{bmatrix} c_1 + c_2 & -c_2 & 0 \\ -c_2 & c_2 + c_3 & -c_3 \\ 0 & -c_3 & c_3 \end{bmatrix}, \quad \mathbf{b} = \frac{1}{m}\begin{Bmatrix} \xi_1 \\ \xi_2 \\ \xi_3 \end{Bmatrix} \tag{2.3}$$

where the parameters c_1, c_2 and c_3 are the respective damping coefficients for the three dashpots. It is straightforward to show that the problem (2.2) can be reduced to a system of two linear differential equations, expressed as

$$\begin{Bmatrix} \dot{u}_1 \\ \dot{u}_2 \end{Bmatrix} + \begin{bmatrix} k_{11} & k_{12} \\ k_{21} & k_{22} \end{bmatrix} \begin{Bmatrix} u_1 \\ u_2 \end{Bmatrix} = \begin{Bmatrix} 0 \\ 0 \end{Bmatrix} \tag{2.4}$$

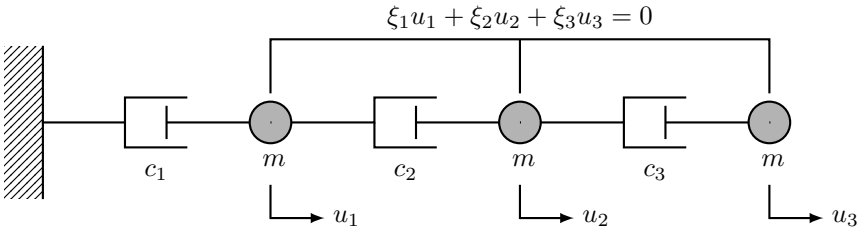

Figure 1: 1D model problem.

where k_{11}, k_{12}, k_{21} and k_{22} depend on the problem parameters. Solving this system yields u_1 and u_2. Subsequently, u_3 is obtained by using the constraint (2.1). The Lagrange multiplier λ can be evaluated by substituting the velocities back into Equation (2.2a). The analytical solutions for $\boldsymbol{u}$ and λ render lengthy terms, which are not shown here for the sake of brevity.

Remark 1: It could be argued that the model problem (2.2) is not fully representative of a viscous incompressible flow problem. However, it possesses very similar characteristics. The masses and dampers of the 1D system are concurrent with the inertial and viscous terms obtained from the Navier-Stokes equations after appropriate discretisation. Moreover, the constraint (2.1) represents well the effect of incompressibility in fluid flow problems, where also a Lagrange multiplier, namely the pressure, is used to impose the linear incompressibility constraint. Due to the absence of an advective component, the model problem is linear and therefore suitable for detailed analyses. In the discretisation of the Navier-Stokes equations the presence of the advection term results in complex eigenvalues of the system matrix. A similar effect can be achieved in the model problem by using complex damping coefficients.

In recent years similar model problems were used successfully, for instance in [15, 17, 16, 29], to study the computational strategies for fluid-structure interaction.

2.2. Time integration schemes

For the purpose of introducing the different time integration schemes, the following general first order differential equation is considered

$$\dot{\boldsymbol{u}} = \boldsymbol{f}(t, \boldsymbol{u}) \tag{2.5}$$

with $\boldsymbol{f}$ being a function of time t and the solution variable $\boldsymbol{u}$.

2.2.1. Backward differentiation formula (BDF)

BDF schemes are implicit linear multi-step methods which allow the derivative of a function to be expressed as a linear combination of solution variables associated with previous time instants. If one considers the differential Equation (2.5) with BDF time integration, the general expression reads

$$\dot{\boldsymbol{u}}^{n+1} = \boldsymbol{f}\big(t^{n+1}, \boldsymbol{u}^{n+1}\big) \tag{2.6}$$

where $\Delta t = t^{n+1} - t^n$ is the time step size, N is the total number of time steps and $n \in \{0, 1, \ldots, N\}$. Depending on the order s of the scheme, the time derivatives of the consequent BDFs scheme are approximated as

$$\dot{\boldsymbol{u}}^{n+1} = \begin{cases} \dfrac{1}{\Delta t}\big(\boldsymbol{u}^{n+1} - \boldsymbol{u}^{n}\big), & \text{for } s = 1 \\ \dfrac{1}{2\Delta t}\big(3\boldsymbol{u}^{n+1} - 4\boldsymbol{u}^{n} + \boldsymbol{u}^{n-1}\big), & \text{for } s = 2 \\ \dfrac{1}{6\Delta t}\big(11\boldsymbol{u}^{n+1} - 18\boldsymbol{u}^{n} + 9\boldsymbol{u}^{n-1} - 2\boldsymbol{u}^{n-2}\big), & \text{for } s = 3 \\ \ldots \end{cases} \tag{2.7}$$

It is observed that, for $s = 1$, the scheme is identical to the backward Euler method (BE). Since only the first order BDF1 and second order BDF2 methods are unconditionally stable, the orders $s > 2$ will be disregarded in this study.

2.2.2. Generalised midpoint rule (GM)

The generalised midpoint rule (GM) can be described as a modified Euler method, which in the case of Equation (2.5) is expressed as

$$\dot{\boldsymbol{u}}^{n+\gamma} = \boldsymbol{f}\left(t^{n+\gamma}, \boldsymbol{u}^{n+\gamma}\right) \tag{2.8}$$

with

$$\dot{\boldsymbol{u}}^{n+\gamma} = \frac{\boldsymbol{u}^{n+1} - \boldsymbol{u}^{n}}{\Delta t} \tag{2.9}$$

$$\boldsymbol{u}^{n+\gamma} = (1-\gamma)\boldsymbol{u}^{n} + \gamma \boldsymbol{u}^{n+1} \tag{2.10}$$

$$t^{n+\gamma} = (1-\gamma)t^{n} + \gamma t^{n+1} \tag{2.11}$$

where γ is a scalar time integration parameter. It can be observed that setting $\gamma = 1/2$ recovers the second order accurate trapezoidal rule (TR), and setting $\gamma = 0$ recovers the backward Euler method (BE/BDF1). Thus the generalised-midpoint rule represents an interpolation between the backward Euler method and the trapezoidal rule. Notably varying γ allows the high frequency damping to be controlled by the user, which is demonstrated clearly in [22, 30]. The limit ρ_{∞}^{h} of the spectral radius as $\Delta t \to \infty$ is related to the parameter γ by

$$\gamma = \frac{1}{1+\rho_{\infty}^{h}} \tag{2.12}$$

The method is unconditionally stable for $1/2 \leq \gamma \leq 1$ which corresponds to $0 \leq \rho_{\infty}^{h} \leq 1$, see [22] or [24] for a thorough explanation.

2.2.3. Generalised-$\boldsymbol{\alpha}$ method (AM)

The generalised-α method is an implicit and unconditionally stable single-step time integration method (see [24, 14]). It is attractive as it allows for high frequency damping to be controlled by the user without jeopardising the second order accuracy. Applying the generalised-α method to the first order problem in Equation (2.5) gives

$$\dot{\boldsymbol{u}}^{n+\alpha_m} = \boldsymbol{f}\left(t^{n+\alpha_f}, \boldsymbol{u}^{n+\alpha_f}\right) \tag{2.13}$$

where

$$\dot{\boldsymbol{u}}^{n+\alpha_m} = (1-\alpha_m)\dot{\boldsymbol{u}}^{n} + \alpha_m \dot{\boldsymbol{u}}^{n+1} \tag{2.14}$$

$$t^{n+\alpha_f} = (1-\alpha_f)t^{n} + \alpha_f t^{n+1} \tag{2.15}$$

$$\boldsymbol{u}^{n+\alpha_f} = (1-\alpha_f)\boldsymbol{u}^{n} + \alpha_f \boldsymbol{u}^{n+1} \tag{2.16}$$

$$\frac{\boldsymbol{u}^{n+1} - \boldsymbol{u}^{n}}{\Delta t} = (1-\gamma)\dot{\boldsymbol{u}}^{n} + \gamma \dot{\boldsymbol{u}}^{n+1} \tag{2.17}$$

The parameters α_m, α_f and γ may be expressed in terms of the spectral radius ρ_{∞}^{h} for an infinitely large time step as follows

$$\alpha_m = \frac{1}{2}\,\frac{3-\rho_{\infty}^{h}}{1+\rho_{\infty}^{h}}, \qquad \alpha_f = \frac{1}{1+\rho_{\infty}^{h}}, \qquad \gamma = \frac{1}{2} + \alpha_m - \alpha_f \tag{2.18}$$

For $\rho_{\infty}^{h} = 0$, the time integration parameters become: $\alpha_m = 3/2$, $\alpha_f = 1$ and $\gamma = 1$, which when applied to Equation (2.13) gives

$$\dot{\boldsymbol{u}}^{n+3/2} = \boldsymbol{f}\left(t^{n+1}, \boldsymbol{u}^{n+1}\right) \tag{2.19}$$

With Equations (2.14) and (2.17), the following is obtained

$$\dot{\boldsymbol{u}}^{n+3/2} = \frac{3\dot{\boldsymbol{u}}^{n+1} - \dot{\boldsymbol{u}}^{n}}{2} = \frac{3\boldsymbol{u}^{n+1} - 4\boldsymbol{u}^{n} + \boldsymbol{u}^{n-1}}{2\Delta t} \tag{2.20}$$

This is identical to the expression in Equation (2.7) for $s = 2$. It can thus be concluded that the generalised-α method with $\rho_\infty^h = 0$ is equivalent to the BDF2 method. This observation is also made in [31]. For $\rho_\infty^h = 1$, the generalised-α method coincides with the trapezoidal rule (TR). Thus, the generalised-α method represents an interpolation between the BDF2 and TR.

2.3. Projection schemes

In the following paragraphs, the time integration techniques of Section 2.2 are employed in the context of projection methods for the simulation of the model problem described in Section 2.1.

The adopted strategy is based on the elimination of the end-of-step velocity, an approach first considered by Guermond and Quartapelle [32, 33, 11]. Furthermore, an incremental projection (or pressure-correction) approach is followed, whereby an approximation of the pressure, or in the context of the model problem (2.2), λ, is included in the first step. This is generally referred to as a pressure-correction method. All schemes presented in the following allow for a varying time step size Δt and for adaptive time stepping.

2.3.1. Generalised-midpoint rule projection method

Typically incremental projection methods are comprised of two steps. The first step, or *viscous* step, contains the viscous contribution of the momentum equation and a predictor for the pressure. In the context of the model problem, the first step of the GM projection method involves the computation of an intermediate velocity at time instant t^{n+1} from

$$\frac{1}{\Delta t}\left(\tilde{\boldsymbol{u}}^{n+1} - \boldsymbol{u}^{n}\right) + \mathbf{C}\tilde{\boldsymbol{u}}^{n+\gamma} + \delta\mathbf{b}\lambda^{*,n+\gamma} = \mathbf{0} \tag{2.21}$$

with

$$\tilde{\boldsymbol{u}}^{n+\gamma} = \gamma\tilde{\boldsymbol{u}}^{n+1} + (1-\gamma)\tilde{\boldsymbol{u}}^{n} \tag{2.22}$$

$$\lambda^{*,n+\gamma} = \gamma\lambda^{*,n+1} + (1-\gamma)\lambda^{n} \tag{2.23}$$

The role of the scalar factor δ is explored further in Section 2.3.3. It is well known that second order accuracy of the overall scheme can be achieved by using a first order predictor for the Lagrange multiplier

$$\lambda^{*,n+1} = \lambda^{n} \tag{2.24}$$

The second step is based on the equations

$$\frac{1}{\Delta t}\left(\boldsymbol{u}^{n+1} - \tilde{\boldsymbol{u}}^{n+1}\right) + \mathbf{b}\left(\lambda^{n+\gamma} - \delta\lambda^{*,n+\gamma}\right) = \mathbf{0} \tag{2.25a}$$

$$\mathbf{b}\cdot\boldsymbol{u}^{n+1} = 0 \tag{2.25b}$$

where

$$\lambda^{n+\gamma} = \gamma\lambda^{n+1} + (1-\gamma)\lambda^{n} \tag{2.26}$$

Crucially, it is observed that the sum of Equations (2.21) and (2.25a) recovers the momentum Equation (2.2a) whereby the inertia term is expressed in terms of the end-of-step velocity $\boldsymbol{u}^{n+1}$ and the viscous term is evaluated for the intermediate velocity $\tilde{\boldsymbol{u}}^{n+1}$. Substituting the expressions (2.23), (2.24) and (2.26) into Equation (2.25a)

renders

$$\frac{1}{\Delta t}\big(\boldsymbol{u}^{n+1} - \tilde{\boldsymbol{u}}^{n+1}\big) + \mathbf{b}\big(\gamma\lambda^{n+1} + (1-\gamma-\delta)\lambda^{n}\big) = \mathbf{0} \tag{2.27}$$

Multiplying Equation (2.27) by $\mathbf{b}$ and recalling Equation (2.25b) results in a scalar equation from which λ^{n+1} can be obtained,

$$-\frac{1}{\Delta t}\mathbf{b}\cdot\tilde{\boldsymbol{u}}^{n+1} + \mathbf{b}\cdot\mathbf{b}\big(\gamma\lambda^{n+1} + (1-\gamma-\delta)\lambda^{n}\big) = \mathbf{0} \tag{2.28}$$

Notably, in the context of the incompressible Navier-Stokes equations, the scalar product with $\mathbf{b}$ corresponds to the application of the divergence operator, which results in a Poisson equation for the pressure increment. The end-of-step velocity $\boldsymbol{u}^{n+1}$ is explicitly computed from Equation (2.27) by substituting λ^{n+1} back into the equation, as follows

$$\boldsymbol{u}^{n+1} = \tilde{\boldsymbol{u}}^{n+1} - \Delta t\mathbf{b}\big(\gamma\lambda^{n+1} + (1-\gamma-\delta)\lambda^{n}\big) \tag{2.29}$$

The second step is generally called the *projection* step since it decomposes the intermediate velocity into the pressure and divergence free end-of-step velocity, as shown in Equations (2.28) and (2.29) respectively.

End-of-step elimination: It is common practice to eliminate the end-of-step velocity from the scheme by substituting the divergence free velocity $\boldsymbol{u}^{n}$, obtained by considering Equation (2.29) at time instant t^n, into the first step (2.21). The explicit step (2.29) is then no longer necessary. Furthermore the intermediate velocity also converges to the exact solution as Δt is reduced. The first step of the GM projection method with end-of-step elimination, from which $\tilde{\boldsymbol{u}}^{n+1}$ is computed, reads

$$\frac{1}{\Delta t}\big(\tilde{\boldsymbol{u}}^{n+1} - \tilde{\boldsymbol{u}}^{n}\big) + \mathbf{C}\tilde{\boldsymbol{u}}^{n+\gamma} + \mathbf{b}\big((\gamma+\delta)\lambda^{n} + (1-\gamma-\delta)\lambda^{n-1}\big) = \mathbf{0} \tag{2.30}$$

The Lagrange multiplier λ^{n+1} is then computed as before from Equation (2.28). There is no need to compute the end-of-step velocity $\boldsymbol{u}^{n+1}$, but if desired it can be evaluated from Equation (2.29).

The system of Equations (2.30) and (2.28) can be expressed in matrix form as

$$\tilde{\mathbf{U}}^{n+1} = \mathbf{A}_{\text{GM}}\tilde{\mathbf{U}}^{n} \tag{2.31}$$

where $\tilde{\mathbf{U}}^{n} = \{\tilde{\boldsymbol{u}}_1^n, \tilde{\boldsymbol{u}}_2^n, \tilde{\boldsymbol{u}}_3^n, \Delta t\lambda^n\}^T$, and $\tilde{\mathbf{U}}^{n+1}$ is expressed analogously. $\mathbf{A}_{\text{GM}}$ is the amplification matrix for the generalised-midpoint rule scheme and its coefficients depend on the problem parameters and on the time step size Δt.

2.3.2. Generalised-$\boldsymbol{\alpha}$ projection method

Adopting the integration scheme presented in Section 2.2.3, and following the approach described in the previous section for the generalised midpoint rule, the first step of the AM projection method, from which $\tilde{\boldsymbol{u}}^{n+1}$ is evaluated, is expressed as

$$\left(1 - \frac{\alpha_m}{\gamma}\right)\dot{\boldsymbol{u}}^{n} + \frac{\alpha_m}{\gamma\Delta t}\big(\tilde{\boldsymbol{u}}^{n+1} - \boldsymbol{u}^{n}\big) + \mathbf{C}\tilde{\boldsymbol{u}}^{n+\alpha_f} + \delta\mathbf{b}\lambda^{*,n+\alpha_f} = \mathbf{0} \tag{2.32}$$

with

$$\tilde{\boldsymbol{u}}^{n+\alpha_f} = \alpha_f\tilde{\boldsymbol{u}}^{n+1} + (1-\alpha_f)\tilde{\boldsymbol{u}}^{n} \tag{2.33}$$

$$\lambda^{*,n+\alpha_f} = \alpha_f\lambda^{*,n+1} + (1-\alpha_f)\lambda^{n} \tag{2.34}$$

where the parameters α_m, α_f and γ are as shown in Equation (2.18), and the predictor $\lambda^{*,n+1}$ is the same as in Equation (2.24).

The second step is obtained as

$$\frac{\alpha_m}{\gamma\Delta t}\big(\boldsymbol{u}^{n+1}-\tilde{\boldsymbol{u}}^{n+1}\big)+\mathbf{b}\big(\lambda^{n+\alpha_f}-\delta\lambda^{*,n+\alpha_f}\big)=\mathbf{0} \tag{2.35a}$$

$$\mathbf{b}\cdot\boldsymbol{u}^{n+1}=0 \tag{2.35b}$$

Similarly to the manipulation of Equation (2.25a), Equation (2.35a) can be rewritten as

$$\frac{\alpha_m}{\gamma\Delta t}\big(\boldsymbol{u}^{n+1}-\tilde{\boldsymbol{u}}^{n+1}\big)+\mathbf{b}\big(\alpha_f\lambda^{n+1}+(1-\alpha_f-\delta)\lambda^n\big)=\mathbf{0} \tag{2.36}$$

Multiplying Equation (2.36) by $\mathbf{b}$ and recalling Equation (2.35b) renders

$$-\frac{\alpha_m}{\gamma\Delta t}\mathbf{b}\cdot\tilde{\boldsymbol{u}}^{n+1}+\mathbf{b}\cdot\mathbf{b}\big(\alpha_f\lambda^{n+1}+(1-\alpha_f-\delta)\lambda^n\big)=\mathbf{0} \tag{2.37}$$

which can be solved for λ^{n+1}. The end-of-step velocity is obtained from

$$\boldsymbol{u}^{n+1}=\tilde{\boldsymbol{u}}^{n+1}-\frac{\gamma\Delta t}{\alpha_m}\mathbf{b}\big(\alpha_f\lambda^{n+1}+(1-\alpha_f-\delta)\lambda^n\big) \tag{2.38}$$

Finally, the acceleration can be computed from

$$\dot{\boldsymbol{u}}^{n+1}=\frac{1}{\gamma\Delta t}\big(\boldsymbol{u}^{n+1}-\boldsymbol{u}^n\big)-\frac{1-\gamma}{\gamma}\dot{\boldsymbol{u}}^n \tag{2.39}$$

End-of-step elimination: The first step of the AM projection method with end-of-step elimination involves computing $\tilde{\boldsymbol{u}}^{n+1}$ from

$$\left(1-\frac{\alpha_m}{\gamma}\right)\dot{\boldsymbol{u}}^n+\frac{\alpha_m}{\gamma\Delta t}\big(\tilde{\boldsymbol{u}}^{n+1}-\tilde{\boldsymbol{u}}^n\big)+\mathbf{C}\tilde{\boldsymbol{u}}^{n+\alpha_f}+\mathbf{b}\big((\alpha_f+\delta)\lambda^n+(1-\alpha_f-\delta)\lambda^{n-1}\big)=\mathbf{0} \tag{2.40}$$

In the second step λ^{n+1} is again computed from (2.37). Substituting the end-of-step velocities $\boldsymbol{u}^n$ and $\boldsymbol{u}^{n+1}$ into Equation (2.39) gives an explicit expression for the end-of-step acceleration

$$\dot{\boldsymbol{u}}^{n+1}=\frac{1}{\gamma\Delta t}\big(\tilde{\boldsymbol{u}}^{n+1}-\tilde{\boldsymbol{u}}^n\big)-\frac{1-\gamma}{\gamma}\dot{\boldsymbol{u}}^n-\frac{1}{\alpha_m}\mathbf{b}\big(\alpha_f\lambda^{n+1}+(1-2\alpha_f-\delta)\lambda^n-(1-\alpha_f-\delta)\lambda^{n-1}\big) \tag{2.41}$$

Since the right hand side contains the acceleration $\dot{\boldsymbol{u}}^n$, it is not possible to use Equation (2.41) to eliminate the end-of-step acceleration in Equation (2.40). Similarly to (2.31), the system of Equations (2.40), (2.37) and (2.41) may be written in matrix form as

$$\tilde{\mathbf{U}}^{n+1}=\mathbf{A}_{\text{AM}}\tilde{\mathbf{U}}^n \tag{2.42}$$

where $\tilde{\mathbf{U}}^n=\{\tilde{\boldsymbol{u}}_1^n,\tilde{\boldsymbol{u}}_2^n,\tilde{\boldsymbol{u}}_3^n,\Delta t\dot{\boldsymbol{u}}_1^n,\Delta t\dot{\boldsymbol{u}}_2^n,\Delta t\dot{\boldsymbol{u}}_3^n,\Delta t\lambda^n\}^T$, and $\tilde{\mathbf{U}}^{n+1}$ can be expressed analogously. $\mathbf{A}_{\text{AM}}$ is the amplification matrix for the generalised-α method.

2.3.3. The role of the factor δ

The factor δ in Equations (2.21) and (2.32) affects the high frequency dissipation of the scheme. A limit analysis of the spectral radius of the amplification matrices $\mathbf{A}_{\text{GM}}$ and $\mathbf{A}_{\text{AM}}$, based on a symbolic mathematics software, yields the following limit

$$\lim_{\Delta t\to\infty}\rho^h=\max(\bar{\rho}_\infty^h,\delta-\bar{\rho}_\infty^h+\delta\bar{\rho}_\infty^h) \tag{2.43}$$

where the parameter $\bar{\rho}_\infty^h$ represents the user-controlled high frequency spectral radius of the applied time integration scheme. Since it is desired that, for the overall method, $\rho^h \to \bar{\rho}_\infty^h$ for $\Delta t \to \infty$, Equation (2.43) suggests to choose δ such that

$$\delta - \bar{\rho}_\infty^h + \delta \bar{\rho}_\infty^h = \bar{\rho}_\infty^h \tag{2.44}$$

which gives

$$\delta = \frac{2\bar{\rho}_\infty^h}{1 + \bar{\rho}_\infty^h} \tag{2.45}$$

Thus, with Equations (2.12), (2.18) and (2.45) the high frequency damping of the GM and AM projection methods presented above can be fully controlled and $\bar{\rho}_\infty^h$ remains as the only free integration parameter. In the case of the GM projection method it can be used to switch gradually between BE and TR. Similarly, in the case of the AM projection method, it allows for interpolation between BDF2 and TR.

2.4. Comparison of schemes

In this section, the projection methods presented in Section 2.3 are compared to each other, as well as to the monolithic and exact solutions discussed in Sections 2.1 and 2.2. First the performance of the schemes is demonstrated for the model problem and subsequently, the schemes are analysed in terms of stability and accuracy.

2.4.1. 1D model problem response

In order to show the capabilities of the GM and AM projection schemes to control high frequency damping, the parameters for the model problem are chosen such that both low and high frequency oscillations are present, and no physical damping occurs. The latter is achieved by choosing imaginary damping coefficients in the matrix $\mathbf{C}$, and the parameters are set as follows: $\xi_1 = 1$, $\xi_2 = 6$, $\xi_3 = 2$, $m = 1$, $c_1 = 0.25i$, $c_2 = 0.32i$, $c_3 = 12i$. By setting the real part of the coefficients to zero, it is ensured that all damping observed in the response of the system is numerical, thus allowing for a straightforward interpretation of the results.

Figure 2 shows the response of the component u_1 when using the GM and AM projection and monolithic schemes with different values of $\bar{\rho}_\infty^h$. The periods associated with the low and high frequencies are, respectively, $T_l = 9.725$ and $T_h = 0.385$. The time step size is chosen as $\Delta t = 0.5 > T_h$. It is desired that, in this case, the unresolved high frequency oscillations are damped out while the low frequencies are accurately captured. For $\bar{\rho}_\infty^h < 1$ it can be seen that the AM projection method more accurately approximates the low frequency response than the GM projection method. Both methods show more numerical dissipation than their monolithic counterparts. As $\bar{\rho}_\infty^h \to 1$, the response experiences less numerical damping and shows more oscillatory behaviour. The numerical oscillations are damped out at a faster rate for the GM method than for the AM method, however at the cost of more low frequency damping. With $\bar{\rho}_\infty^h = 1$, the TR projection method is recovered, and as expected there is no numerical damping observed for the high or low frequencies.

2.4.2. 1D model problem spectral radii

The spectral radius of a scheme's amplification matrix is defined for a $d \times d$ matrix as

$$\rho^h(\mathbf{A}) = \max(|\lambda_1|, |\lambda_2|, \ldots, |\lambda_d|) \tag{2.46}$$

where $\lambda_{1,2,\ldots,d}$ represent the eigenvalues of the amplification matrix of dimension d and must not be confused with the Lagrange multiplier for the constraint. For a scheme to be unconditionally stable, the spectral radius must not exceed 1 for all positive time step sizes Δt, i.e. $\rho^h(\mathbf{A}) \leq 1 \; \forall \; \Delta t \geq 0$. Since $\rho^h(\mathbf{A})$ is highly nonlinear with respect to Δt, only the limits of $\rho^h(\mathbf{A})$ for $\Delta t \to 0$ and $\Delta t \to \infty$ can be obtained analytically while, for any given finite value of Δt, the stability check is restricted to the numerical investigation for the given parameters.

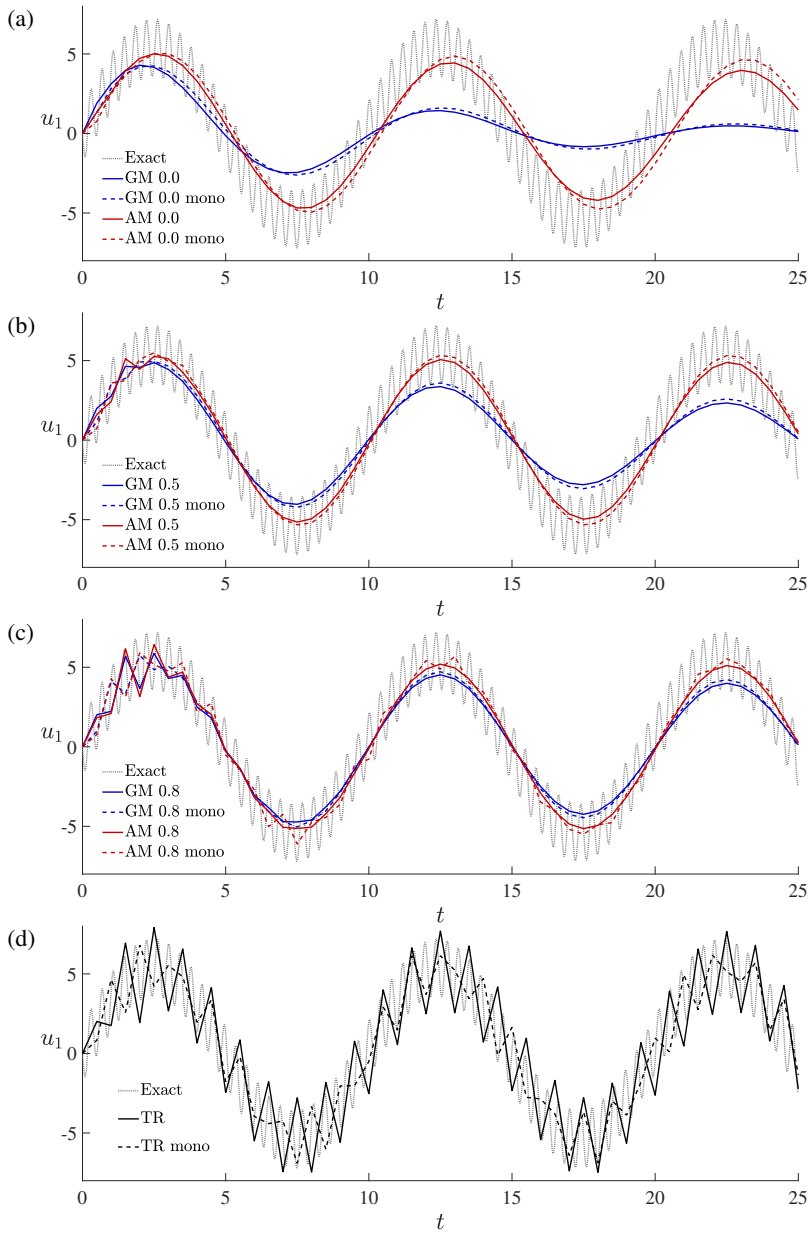

Figure 2: 1D model problem: u_1 response for the GM and AM projection methods with (a) $\bar{\rho}^h_\infty = 0$, (b) $\bar{\rho}^h_\infty = 0.5$, (c) $\bar{\rho}^h_\infty = 0.8$, and (d) $\bar{\rho}^h_\infty = 1$, i.e. TR projection method.

The spectral radii for the GM and AM projection methods are compared to their respective monolithic counterparts as well as to the monolithic BE method in Figure 3, using the same parameters as in Section 2.4.1. It is visible for both methods that $\rho^h \leq 1$ for all values of $\bar{\rho}^h_\infty$ chosen. It is also evident that $\bar{\rho}^h_\infty$ in both cases defines the limit of the high frequency damping ρ^h_∞.

The direct comparison between the GM and AM projection methods is shown in Figure 4. Notably, for any value of $\bar{\rho}^h_\infty$ the AM projection method displays less numerical damping in the lower frequency range than the GM projection method. It is also observed that for $\bar{\rho}^h_\infty = 0$ the AM projection scheme is less dissipative than the monolithic BE method. A similar comparison involving only the monolithic counterparts of the methods is presented in Figure 5.

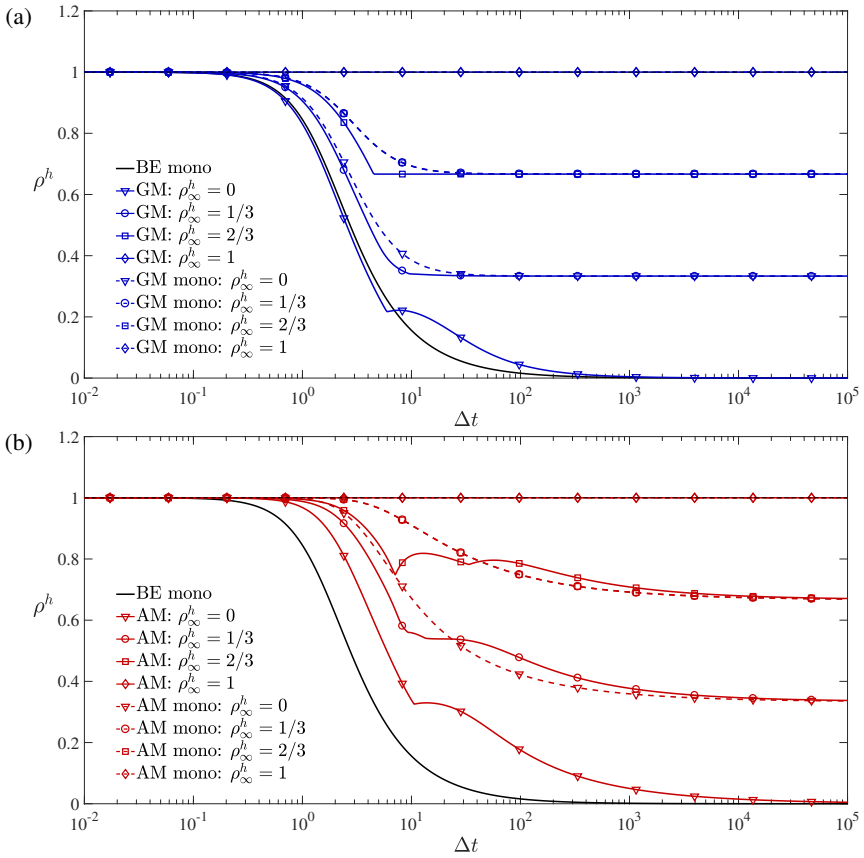

Figure 3: 1D model problem: Spectral radius comparison between the GM projection and monolithic methods (a), and the AM projection and monolithic methods (b), using a range of values for $\bar{\rho}^h_\infty$.

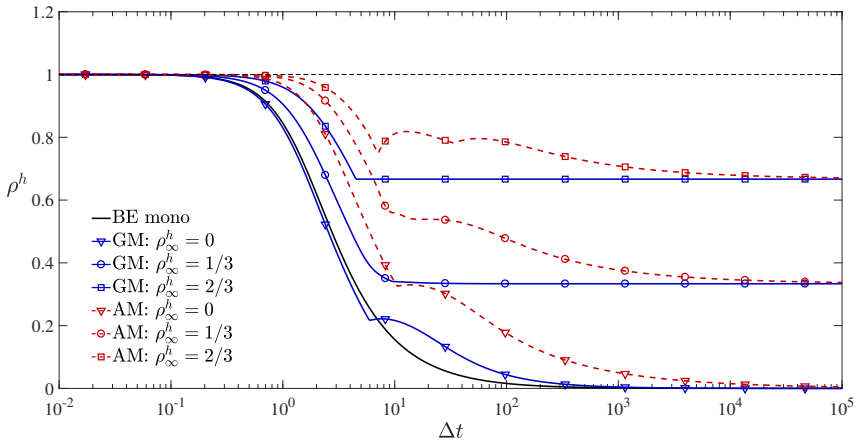

Figure 4: 1D model problem: Spectral radius comparison between the GM and AM projection methods.

Figure 6 shows the spectral radii as obtained from modified versions of the proposed GM and AM projection schemes, where $\delta = 1$. Thus, Step 1 of the modified schemes includes a full predictor for the Lagrange multiplier λ. It is evident that the high frequency damping is lost and $\rho^h_\infty = 1$ is recovered in all cases. However, similarly to their monolithic counterparts, the modified schemes exhibit less damping in the low frequency range.

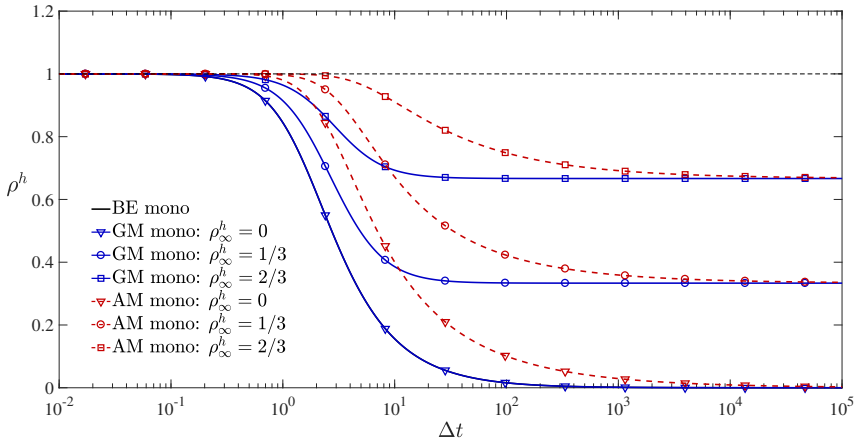

Figure 5: 1D model problem: Spectral radius comparison between the monolithic GM and AM methods.

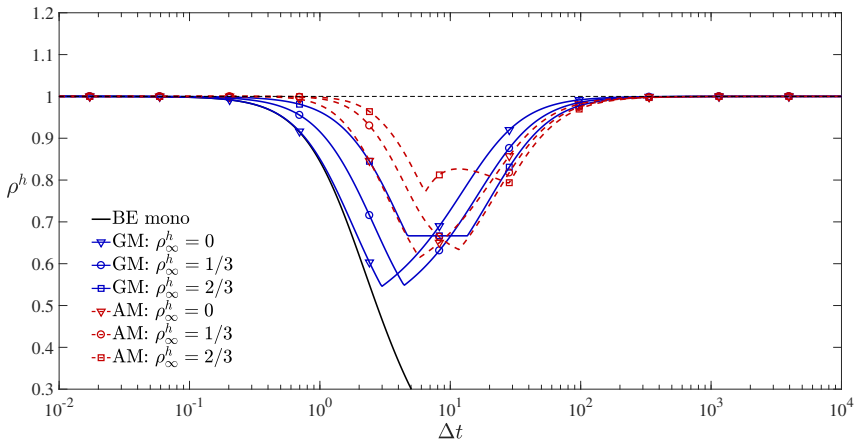

Figure 6: 1D model problem: Spectral radius comparison between the modified GM and AM projection methods with $\delta = 1$.

2.4.3. 1D model problem convergence

The convergence of the solution variables as Δt decreases is shown in Figure 7. The parameters are set as: $\xi_1 = 1$, $\xi_2 = 1$, $\xi_3 = 1$, $m = 1$, $c_1 = 1i$, $c_2 = 1i$ and $c_3 = 1i$. The errors are obtained by comparison to the exact solution at time instant $t = 30$. With $\bar{\rho}^h_\infty = 0$ and $\bar{\rho}^h_\infty = 0.5$, first order accuracy is observed for both the GM and AM projection methods. However, the AM projection method shows a smaller magnitude of error. Moreover, for $\bar{\rho}^h_\infty = 0.5$, the convergence slope of the AM projection method begins to increase towards second order accuracy at larger time steps. For $\bar{\rho}^h_\infty = 1$, the second order accurate TR method is recovered. It can be deduced that increasing $\bar{\rho}^h_\infty$ effectively reduces the magnitude of the error for both methods.

It is pointed out that second order accuracy is achieved for all values of $\bar{\rho}^h_\infty$ with the AM projection method by setting $\delta = 1$ in (2.40). However, as shown in Section 2.4.2, this is associated with the loss of high frequency damping.

A further comparison of the GM and AM projection methods is shown in Figure 8, where the solution errors are shown for the range $0 \leq \bar{\rho}^h_\infty \leq 1$. Notably for $\bar{\rho}^h_\infty < 0.9$, the AM projection method is an order of magnitude more accurate than the GM projection method.

2.5. Conclusions drawn from model problem analysis

Based on the observations made in Section 2.4, the following conclusions can be drawn:

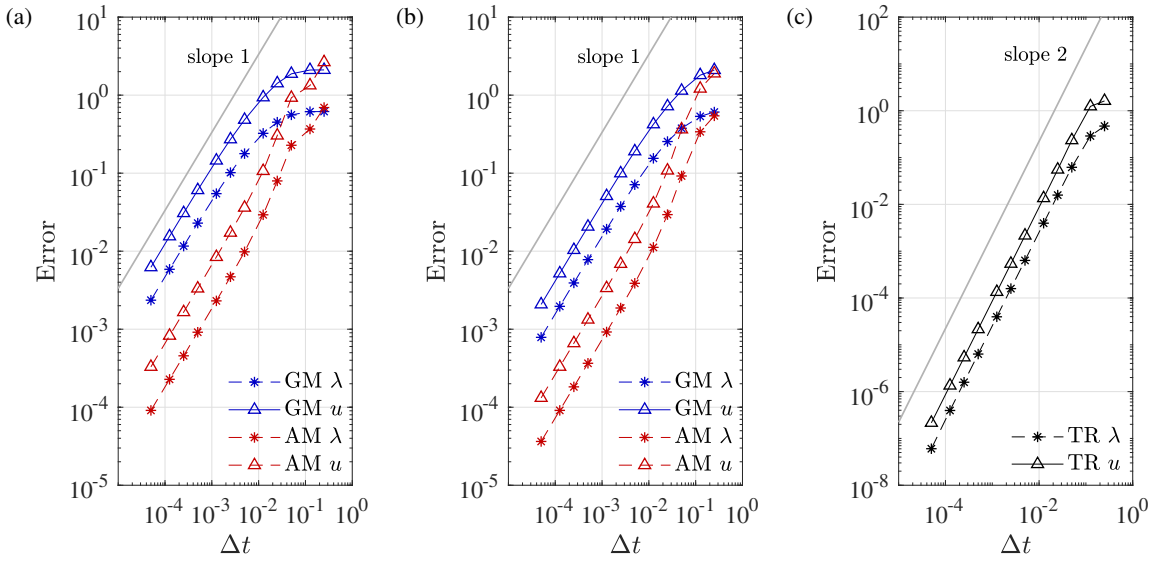

Figure 7: 1D model problem: $\text{Error}(\boldsymbol{u}) = \sqrt{(u_1 - u_{1,\text{ex}})^2 + (u_2 - u_{2,\text{ex}})^2 + (u_3 - u_{3,\text{ex}})^2}$ and $\text{Error}(\lambda) = |\lambda - \lambda_{\text{ex}}|$ for (a) $\bar{\rho}_\infty^h = 0$, (b) $\bar{\rho}_\infty^h = 0.5$ and (c) $\bar{\rho}_\infty^h = 1$, at $t = 30$. The terms $(\bullet)_{\text{ex}}$ denote the analytical solution.

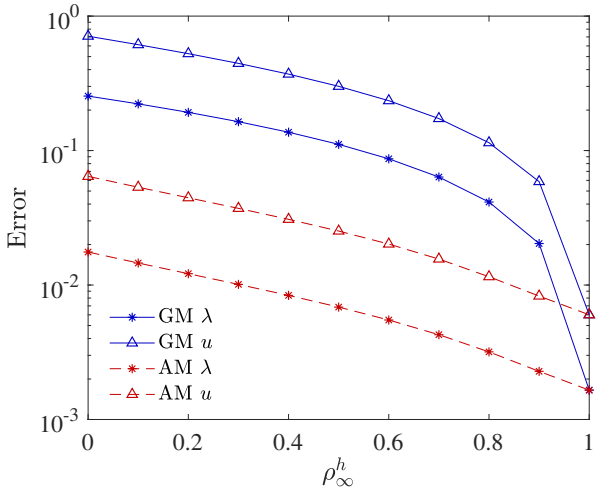

Figure 8: 1D model problem: Comparison of errors obtained for different values of $\bar{\rho}_\infty^h$. The errors are evaluated at $\Delta t = 0.01$.

(i) The standard projection method based on the backward Euler time integration scheme which does not involve a pressure term in the first step features the same high frequency damping as its monolithic counterpart, i.e. $\rho_\infty^h \to 0$ for $\Delta t \to \infty$.

(ii) The widely used pressure correction method based on BDF2, which includes a pressure predictor in the first step and which maintains second order accuracy, does not feature any high frequency damping, i.e. $\rho_\infty^h \to 1$ for $\Delta t \to \infty$. This is in stark contrast to its monolithic counterpart where $\rho_\infty^h \to 0$ for $\Delta t \to \infty$.

(iii) In the proposed GM and AM projection schemes, the parameters δ and $\bar{\rho}_\infty^h$ control high frequency damping according to Equation (2.43).

(iv) The investigation confirms the well-known fact that overall second order accuracy can only be obtained for $\delta = 1$. Together with Conclusion (iii), this suggests that it is not possible to formulate a second order accurate pressure correction method which possesses any high frequency damping.

(v) The proposed AM scheme features only first order accuracy, but renders significantly more accurate results than the standard backward Euler projection method or indeed the proposed GM scheme. The additional computational cost associated with the proposed AM scheme is negligible. Similarly to its monolithic counterpart it provides the desired high frequency damping while preserving the resolved low frequency response.

3. Formulations for incompressible fluid flow

In this section the projection methods proposed in Section 2 will be applied to the incompressible Navier-Stokes equations.

Consider a domain $\Omega \subset \mathbb{R}^d$ ($d \leq 3$) with boundary Γ which is separable into Dirichlet and Neumann subsets, Γ_D and Γ_N. The velocity field $\boldsymbol{u}$ and pressure field p are described by the following governing equations

$$\rho(\dot{\boldsymbol{u}} + (\boldsymbol{u} \cdot \nabla)\boldsymbol{u}) - \nabla \cdot \boldsymbol{\sigma} = \boldsymbol{f} \qquad \text{in } \Omega \times [0,T] \tag{3.1a}$$

$$\nabla \cdot \boldsymbol{u} = 0 \qquad \text{in } \Omega \times [0,T] \tag{3.1b}$$

$$\boldsymbol{u} = \boldsymbol{u}_D \qquad \text{on } \Gamma_D \times [0,T] \tag{3.1c}$$

$$\boldsymbol{\sigma} \cdot \boldsymbol{n} = \boldsymbol{t} \qquad \text{on } \Gamma_N \times [0,T] \tag{3.1d}$$

$$\boldsymbol{u}|_{t=0} = \boldsymbol{u}_0 \qquad \text{in } \Omega \tag{3.1e}$$

where $[0,T]$ is the time interval under consideration, $\boldsymbol{f}$ is the body force vector, $\boldsymbol{u}_D$ is the velocity prescribed on Γ_D, $\boldsymbol{n}$ is the outward normal to Γ, $\boldsymbol{\sigma}$ is the Cauchy stress tensor, and $\boldsymbol{t}$ is the imposed boundary traction. Using the definition of the symmetric gradient, $\nabla^s := \frac{1}{2}(\nabla + \nabla^T)$, and of the Cauchy stress tensor for Newtonian fluids

$$\boldsymbol{\sigma} = -p\boldsymbol{I} + 2\mu\nabla^s\boldsymbol{u} \tag{3.2}$$

in Equation (3.1a) renders

$$\rho(\dot{\boldsymbol{u}} + (\boldsymbol{u} \cdot \nabla)\boldsymbol{u}) - \mu\Delta\boldsymbol{u} + \nabla p = \boldsymbol{f} \tag{3.3}$$

3.1. Projection schemes: time discretisation

Analogously to Section 2.3, GM and AM projection schemes are proposed for the Navier-Stokes Equations (3.1a)-(3.1e). The nonlinearity of the convection term is avoided by extrapolating the convective velocity $\boldsymbol{u}^{*,n+1}$ from the solution history in an appropriate manner.

3.1.1. GM projection method

The method to be presented is based on the same strategy used in Section 2.3.1, specifically Equations (2.30) and (2.28). The first step of the GM projection method with end-of-step elimination involves the computation of the intermediate velocity, $\tilde{\boldsymbol{u}}$, at time instance t^{n+1} from

$$\begin{aligned}\frac{\rho}{\Delta t}\big(\tilde{\boldsymbol{u}}^{n+1} - \tilde{\boldsymbol{u}}^{n}\big) + \rho\big(\tilde{\boldsymbol{u}}^{*,n+\gamma} \cdot \nabla\big)\tilde{\boldsymbol{u}}^{n+\gamma} + \mu\Delta\tilde{\boldsymbol{u}}^{n+\gamma} \\ + \nabla\big((\gamma+\delta)p^{n} + (1-\gamma-\delta)p^{n-1}\big) = \boldsymbol{f}^{n+\gamma}\end{aligned} \tag{3.4a}$$

$$\tilde{\boldsymbol{u}}^{n+1}|_{\Gamma_D} = \boldsymbol{u}_D^{n+1} \tag{3.4b}$$

with

$$\tilde{\boldsymbol{u}}^{*,n+\gamma} = \gamma\tilde{\boldsymbol{u}}^{*,n+1} + (1-\gamma)\tilde{\boldsymbol{u}}^{n} \tag{3.5}$$

$$\tilde{\boldsymbol{u}}^{n+\gamma} = \gamma\tilde{\boldsymbol{u}}^{n+1} + (1-\gamma)\tilde{\boldsymbol{u}}^{n} \tag{3.6}$$

$$\boldsymbol{f}^{n+\gamma} = \gamma\boldsymbol{f}^{n+1} + (1-\gamma)\boldsymbol{f}^{n} \tag{3.7}$$

Here the parameters γ and δ are obtained from Equations (2.12) and (2.45) respectively. The convective velocity extrapolation is expressed as

$$\tilde{\boldsymbol{u}}^{*,n+1} = 2\tilde{\boldsymbol{u}}^{n} - \tilde{\boldsymbol{u}}^{n-1} \tag{3.8}$$

Equation (3.4a) resembles Equation (2.30), with λ being replaced by the pressure p and the addition of a convection term. The second order extrapolation in Equation (3.8) is not necessary for $\bar{\rho}_\infty^h < 1$, but crucial to ensure second order accuracy for $\bar{\rho}_\infty^h = 1$ (TR). The second step of the GM projection method is based on

$$\frac{\rho}{\Delta t}\big(\boldsymbol{u}^{n+1} - \tilde{\boldsymbol{u}}^{n+1}\big) + \nabla\big(\gamma p^{n+1} + (1-\gamma-\delta)p^{n}\big) = \boldsymbol{0} \tag{3.9a}$$

$$\nabla\cdot\boldsymbol{u}^{n+1} = 0 \tag{3.9b}$$

$$\boldsymbol{u}^{n+1}\cdot\boldsymbol{n}|_{\Gamma_D} = 0 \tag{3.9c}$$

Taking the divergence of the terms in Equation (3.9a) and applying Equation (3.9b) yields the following Poisson equation for p^{n+1}

$$-\frac{\rho}{\Delta t}\nabla\cdot\tilde{\boldsymbol{u}}^{n+1} + \Delta\big(\gamma p^{n+1} + (1-\gamma-\delta)p^{n}\big) = 0 \tag{3.10}$$

3.1.2. Generalised-α projection method

Following the same strategy as for Equations (2.40) and (2.37) in Section 2.3.2, the first step of the AM projection method with end-of-step elimination requires to compute $\tilde{\boldsymbol{u}}^{n+1}$ from

$$\begin{aligned}\rho\left(1-\frac{\alpha_m}{\gamma}\right)\dot{\boldsymbol{u}}^{n} + \frac{\rho\alpha_m}{\gamma\Delta t}\big(\tilde{\boldsymbol{u}}^{n+1} - \tilde{\boldsymbol{u}}^{n}\big) + \rho\big(\tilde{\boldsymbol{u}}^{*,n+\alpha_f}\cdot\nabla\big)\tilde{\boldsymbol{u}}^{n+\alpha_f} + \mu\Delta\tilde{\boldsymbol{u}}^{n+\alpha_f} \\ + \nabla\big((\alpha_f+\delta)p^{n} + (1-\alpha_f-\delta)p^{n-1}\big) = \boldsymbol{f}^{n+\alpha_f}\end{aligned} \tag{3.11a}$$

$$\tilde{\boldsymbol{u}}^{n+1}|_{\Gamma_D} = \boldsymbol{u}_D^{n+1} \tag{3.11b}$$

with

$$\tilde{\boldsymbol{u}}^{*,n+\alpha_f} = \alpha_f\tilde{\boldsymbol{u}}^{*,n+1} + (1-\alpha_f)\tilde{\boldsymbol{u}}^{n} \tag{3.12}$$

$$\tilde{\boldsymbol{u}}^{n+\alpha_f} = \alpha_f\tilde{\boldsymbol{u}}^{n+1} + (1-\alpha_f)\tilde{\boldsymbol{u}}^{n} \tag{3.13}$$

$$\boldsymbol{f}^{n+\alpha_f} = \alpha_f\boldsymbol{f}^{n+1} + (1-\alpha_f)\boldsymbol{f}^{n} \tag{3.14}$$

where the parameters α_m, α_f and γ are given in Equation (2.18), and the convective velocity extrapolation is the same as in Equation (3.8).

In the second step the relations

$$\frac{\rho\alpha_m}{\gamma\Delta t}\big(\boldsymbol{u}^{n+1}-\tilde{\boldsymbol{u}}^{n+1}\big)+\nabla\big(\alpha_f p^{n+1}+(1-\alpha_f-\delta)p^n\big)=\boldsymbol{0} \tag{3.15}$$

$$\nabla\cdot\boldsymbol{u}^{n+1}=0 \tag{3.16}$$

$$\boldsymbol{u}^{n+1}\cdot\boldsymbol{n}|_\Gamma=0 \tag{3.17}$$

render the following Poisson equation for the pressure p^{n+1}

$$-\frac{\rho\alpha_m}{\gamma\Delta t}\nabla\cdot\tilde{\boldsymbol{u}}^{n+1}+\Delta\big(\alpha_f p^{n+1}+(1-\alpha_f-\delta)p^n\big)=0 \tag{3.18}$$

The acceleration is computed from

$$\begin{aligned}\rho\dot{\boldsymbol{u}}^{n+1}=&\frac{\rho}{\gamma\Delta t}\big(\tilde{\boldsymbol{u}}^{n+1}-\tilde{\boldsymbol{u}}^{n}\big)-\rho\frac{1-\gamma}{\gamma}\dot{\boldsymbol{u}}^n\\&-\frac{1}{\alpha_m}\nabla\big(\alpha_f p^{n+1}+(1-2\alpha_f-\delta)p^n-(1-\alpha_f-\delta)p^{n-1}\big)\end{aligned} \tag{3.19}$$

3.2. Finite element method: spatial discretisation

The spatial discretisation is based on the following velocity and pressure interpolation and weighting functions

$$\boldsymbol{u}^h(\boldsymbol{x})=\sum_{A\in\eta}N_A(\boldsymbol{x})\boldsymbol{u}_A,\quad \boldsymbol{v}^h(\boldsymbol{x})=\sum_{A\in\eta}N_A(\boldsymbol{x})\boldsymbol{v}_A \tag{3.20}$$

$$p^h(\boldsymbol{x})=\sum_{\tilde{A}\in\tilde{\eta}}\tilde{N}_{\tilde{A}}(\boldsymbol{x})p_{\tilde{A}},\quad q^h(\boldsymbol{x})=\sum_{\tilde{A}\in\tilde{\eta}}\tilde{N}_{\tilde{A}}(\boldsymbol{x})q_{\tilde{A}} \tag{3.21}$$

where η and $\tilde{\eta}$, A and $\tilde{A}$, N_A and $\tilde{N}_{\tilde{A}}$ represent, respectively, the sets of nodes, the global node numbers and the shape functions for velocity and pressure.

For a compact presentation of the weak forms to be used for the computations in Steps 1 and 2 of the proposed schemes, it is useful to define the following integral forms

$$(\boldsymbol{u},\boldsymbol{v})=\int_\Omega\boldsymbol{u}\cdot\boldsymbol{v}\,d\Omega \tag{3.22}$$

$$a(\boldsymbol{u},\boldsymbol{v})=\mu\int_\Omega\nabla\boldsymbol{u}:\nabla\boldsymbol{v}\,d\Omega \tag{3.23}$$

$$b(\boldsymbol{v},q)=-\int_\Omega q\nabla\cdot\boldsymbol{v}\,d\Omega \tag{3.24}$$

$$c(\boldsymbol{u},\boldsymbol{v},\boldsymbol{w})=\rho\int_\Omega(\boldsymbol{u}\cdot\nabla\boldsymbol{u})\cdot\boldsymbol{w}\,d\Omega \tag{3.25}$$

GM projection method: The first step requires to solve the weak form of Equation (3.4) for the intermediate velocity: Find $\tilde{\boldsymbol{u}}^{n+1}\in\tilde{\mathcal{S}}$, such that for all $\boldsymbol{v}\in\tilde{\mathcal{V}}$

$$\begin{aligned}\left(\rho\frac{\tilde{\boldsymbol{u}}^{n+1}-\tilde{\boldsymbol{u}}^{n}}{\Delta t},\boldsymbol{v}\right)&+a\big(\tilde{\boldsymbol{u}}^{n+\gamma},\boldsymbol{v}\big)+c\big(\tilde{\boldsymbol{u}}^{*,n+\gamma},\tilde{\boldsymbol{u}}^{n+\gamma},\boldsymbol{v}\big)\\&+b\big(\boldsymbol{v},(\gamma+\delta)p^n+\big(1-\gamma-\delta\big)p^{n-1}\big)=\big(\boldsymbol{f}^{n+\gamma},\boldsymbol{v}\big)\end{aligned} \tag{3.26}$$

where $\tilde{\mathcal{S}}$ and $\tilde{\mathcal{V}}$ represent the appropriate finite element approximation spaces and the superscript h has been

omitted. The quantities $\tilde{\boldsymbol{u}}^{*,n+\gamma}$, $\tilde{\boldsymbol{u}}^{n+\gamma}$ and $\boldsymbol{f}^{n+\gamma}$ are obtained from Equations (3.5)-(3.7). The Dirichlet boundary conditions are applied directly to the intermediate velocity $\tilde{\boldsymbol{u}}$.

The Poisson Equation (3.10) yields the following weak formulation: Find $p^{n+1} \in \mathcal{P}$, such that for all $q \in \mathcal{P}$

$$\big(\nabla\big(\gamma p^{n+1} + \big(1-\gamma-\delta\big)p^n\big), \nabla q\big) = \frac{\rho}{\Delta t} b\big(\tilde{\boldsymbol{u}}^{n+1}, q\big) \tag{3.27}$$

where $\mathcal{P}$ represents the appropriate finite element approximation space.

AM projection method: The weak form of Equation (3.11) in the first step reads: Find $\tilde{\boldsymbol{u}}^{n+1} \in \tilde{\mathcal{S}}$, such that for all $\boldsymbol{v} \in \tilde{\mathcal{V}}$

$$\begin{aligned}\left(\rho\left(\dot{\boldsymbol{u}}^n\left(1-\frac{\alpha_m}{\gamma}\right) + \alpha_m \frac{\tilde{\boldsymbol{u}}^{n+1}-\tilde{\boldsymbol{u}}^n}{\gamma\Delta t}\right), \boldsymbol{v}\right) + a\big(\tilde{\boldsymbol{u}}^{n+\alpha_f}, \boldsymbol{v}\big) + c\big(\tilde{\boldsymbol{u}}^{*,n+\alpha_f}, \tilde{\boldsymbol{u}}^{n+\alpha_f}, \boldsymbol{v}\big) \\ + b\big(\boldsymbol{v}, (\alpha_f+\delta)p^n + \big(1-\alpha_f-\delta\big)p^{n-1}\big) = \big(\boldsymbol{f}^{n+\alpha_f}, \boldsymbol{v}\big)\end{aligned} \tag{3.28}$$

The weak form of Equation (3.18) is expressed as: Find $p^{n+1} \in \mathcal{P}$, such that for all $q \in \mathcal{P}$

$$\big(\nabla\big(\alpha_f p^{n+1} + \big(1-\alpha_f-\delta\big)p^n\big), \nabla q\big) = \frac{\rho\alpha_m}{\gamma\Delta t} b\big(\tilde{\boldsymbol{u}}^{n+1}, q\big) \tag{3.29}$$

The acceleration update from Equation (3.19) is obtained from

$$\begin{aligned}\big(\rho\dot{\boldsymbol{u}}^{n+1}, \boldsymbol{v}\big) = \left(\rho\frac{\tilde{\boldsymbol{u}}^{n+1}-\tilde{\boldsymbol{u}}^n}{\gamma\Delta t}, \boldsymbol{v}\right) - \left(\frac{1-\gamma}{\gamma}\rho\dot{\boldsymbol{u}}^n, \boldsymbol{v}\right) \\ - b\left(\boldsymbol{v}, \frac{1}{\alpha_m}\big(\alpha_f p^{n+1} + (1-2\alpha_f-\delta)p^n - (1-\alpha_f-\delta)p^{n-1}\big)\right)\end{aligned} \tag{3.30}$$

It should be noted that, if the product of the mass matrix with the nodal accelerations is employed as history variable, then Equation (3.30) is explicit and its computational cost negligible. This is consistent with Equation (3.28) which also involves the product of the $\dot{\boldsymbol{u}}$ with the mass matrix.

3.3. Stable velocity-pressure interpolations

It is well-known that a pure Galerkin based mixed velocity-pressure finite element formulation for the incompressible Navier-Stokes equations renders spurious oscillations in the pressure field if the same interpolation functions are used for the velocity and the pressure fields. Admissible choices of approximation spaces are required to satisfy the inf-sup condition

$$\inf_{\boldsymbol{q}^h \in \mathcal{P}^h} \sup_{\boldsymbol{v}^h \in \mathcal{V}^h} \frac{(\nabla \cdot \boldsymbol{v}^h, \boldsymbol{q}^h)}{\|\boldsymbol{q}\|_0 \|\boldsymbol{v}^h\|_1} \geq \alpha > 0 \tag{3.31}$$

where α is a constant, which is indepensent of the element size. Inequality (3.31) is also known as the LBB compatibility condition [34, 35, 36, 37, 38]. Alternatively, appropriate stabilisation techniques can be employed which are based on variants of the Galerkin method and thereby circumvent the condition. Prominent techniques such as the SUPG/PSPG stabilisation technique or Least-squares finite element method have been widely used and further developed (see, for instance, [39, 40, 41, 42, 43, 44]). It is interesting that, in the context of projection schemes, smooth pressure fields may be obtained even without stabilisation or inf-sup conformity. This is due to the fact that, for large time steps, the incompressibility constraint is far less rigorously enforced. However, it has now become common practice to employ inherently stable velocity-pressure formulations in order to ensure maximum robustness of the overall methodology (see for instance [33, 45]). Similarly to the issue of high-frequency damping addressed in this work, a stable velocity-pressure formulation is crucial to allow for a large degree of independence between spatial and temporal discretisations. Thus, the well-known inf-sup stable

Taylor-Hood element (P_2/P_1) based on quadratic velocity and linear pressure triangular elements is employed in the numerical examples in Section 4.

4. Numerical examples

4.1. Lid-driven cavity

As a first demonstration, the benchmark flow problem of a lid-driven cavity is considered. The side length of the square cavity is one unit length and the boundary conditions are shown in Figure 9. The no-slip boundary condition is applied to all edges except at the lid boundary, where the normal velocity component is set to zero and the tangential velocity component follows the profile

$$u_{\text{lid}}(x) = 1 - \mathrm{e}^{a(x-1)} - \mathrm{e}^{-ax} \qquad 0 \leq x \leq 1 \tag{4.1}$$

where a is a dimensionless parameter and x is the horizontal coordinate (adopted from Dettmer *et al.*[46]). The profile (4.1) allows for the control of the sharpness of the singularity in the top corners of the cavity. For this demonstration, $a = 50$ is used. Two Reynolds numbers are tested, $Re = 100$ and $Re = 1000$, which result from using viscosities of $\mu = 0.01$ and $\mu = 0.001$ respectively and a density of $\rho = 1$. Three unstructured meshes are considered: mesh A (847 elements, 1782 P_2 nodes), mesh B (2061 elements, 4260 P_2 nodes) and mesh C (4200 elements, 8597 P_2 nodes). Mesh A is shown in Figure 9. Initially the fluid is at rest and the velocity at the lid is applied instantaneously. The GM projection scheme with $\bar{\rho}^h_\infty = 0$ is used.

The steady state solutions shown in Figures 10-12 develop quickly and agree well with the reference solutions. The streamlines and pressure contours are shown for $Re = 100$ and $Re = 1000$ in Figures 10 and 11, respectively. Figure 12a shows the horizontal velocity component u and the vertical velocity component v along the vertical and horizontal centrelines of the cavity respectively for $Re = 100$. Similarly the centreline velocities for $Re = 1000$ are shown in Figure 12b.

4.2. Lid-driven cavity with dynamic boundary conditions

For the purpose of studying the convergence of the projection schemes, the lid driven cavity problem is considered once more. In order to avoid a steady state solution, the velocity profile in Equation (4.1) is replaced by the time dependant profile

$$u_{\text{lid}}(x,t) = \frac{1}{2}\sin(\pi x)\big(1 - \cos(3\pi t)\big) \tag{4.2}$$

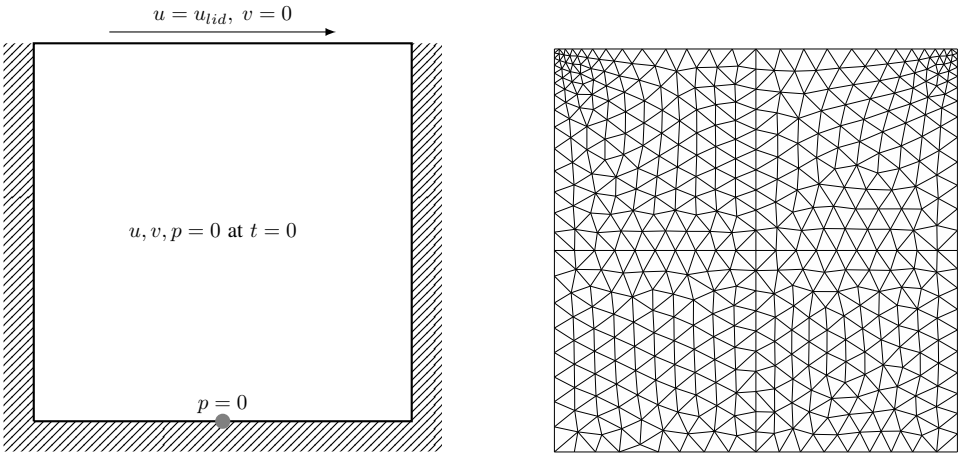

Figure 9: Lid-driven cavity: Boundary conditions and mesh A

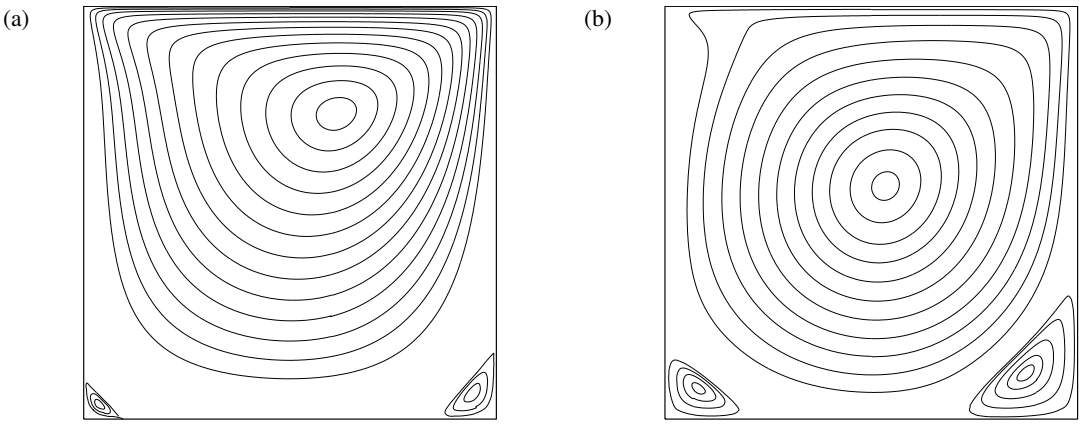

Figure 10: Lid-driven cavity: Streamlines for $Re = 100$ (a) and $Re = 1000$ (b).

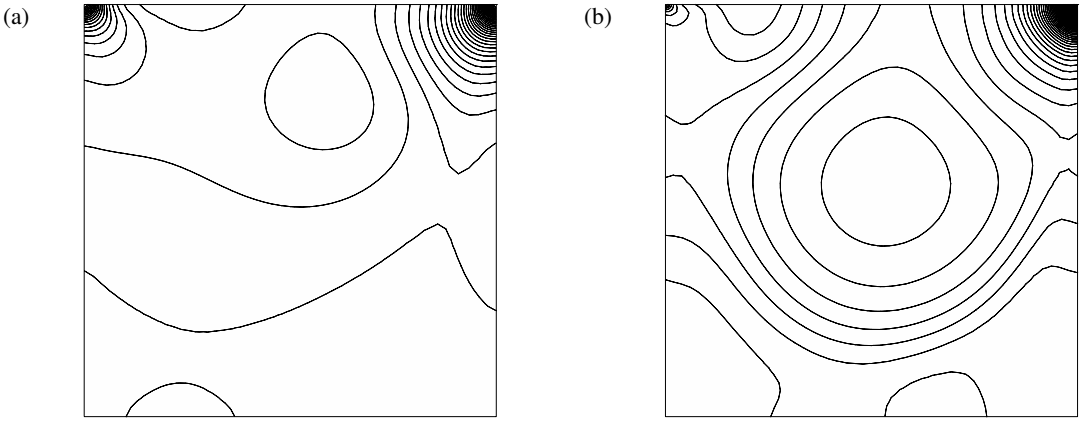

Figure 11: Lid-driven cavity: Pressure isolines for $Re = 100$ (a) and $Re = 1000$ (b).

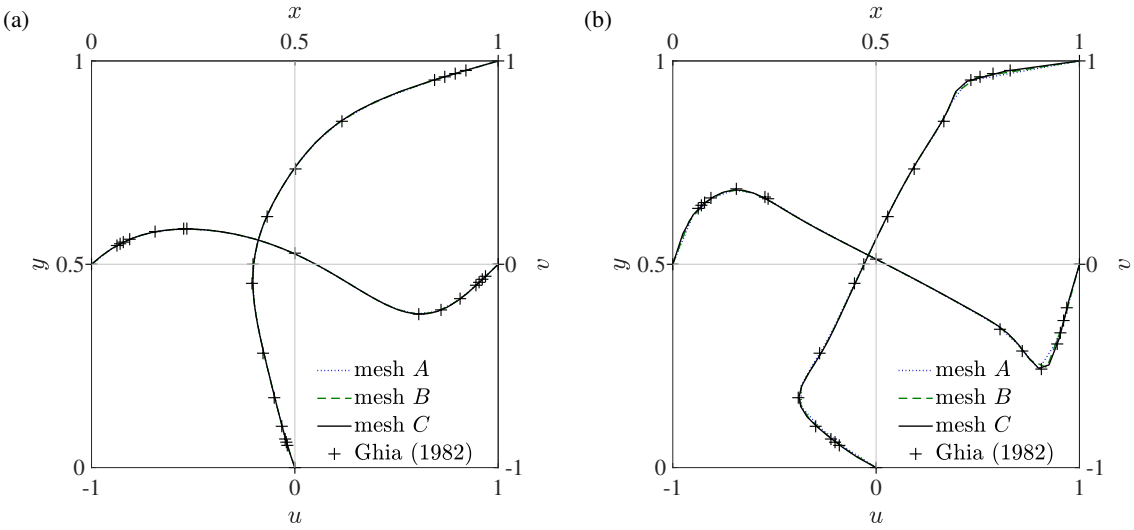

Figure 12: Lid-driven cavity: Horizontal velocity u along the vertical centreline and vertical velocity v along the horizontal centreline, for $Re = 100$ (a) and $Re = 1000$ (b).

In the convergence analyses to follow, the problem is run until $t = 1$. The viscosity and density are respectively set to $\mu = 0.0025$ and $\rho = 1$ resulting in $Re = 400$, and a mesh with 1140 elements (2365 P_2 nodes) is used. It is demonstrated that, as the time step size Δt is reduced while the spatial discretisation remains unchanged, the velocity and pressure fields converge to an exclusively mesh-dependent approximation of the exact solution. It is shown that, for the same spatial discretisation, the GM and AM projection schemes and the monolithic solver converge to the same response. The reference responses for the Stokes problem in Section 4.2.1 and for the Navier-Stokes problem in Section 4.2.2 have been computed with the corresponding monolithic AM solvers based on $\Delta t = 0.0001$. The term "error" is used for the deviation between the reference solution and the solutions obtained with the GM and AM projection schemes on the same mesh but for various values of Δt. Similar studies of temporal convergence have been performed in [22, 32, 33, 45] in the context of different methodologies.

4.2.1. Error convergence for Stokes problem

The convergence rates of the L^2 error norms of the velocity and pressure fields are shown for the Stokes flow problem in Figure 13, where the GM and AM projection methods are compared. It is clear that for $\bar{\rho}^h_\infty = 0$, the GM and AM projection methods obtain first order convergence rates for both the velocity and pressure field errors. Although both methods are first order accurate in time, the AM projection method produces a smaller magnitude of error for both velocity and pressure fields. For $\rho^h_\infty = 0.5$, both methods again obtain first order accuracy, although the convergence slope increases towards second order accuracy for larger time steps. Again, the AM projection method performs better in terms of the error magnitude. For $\bar{\rho}^h_\infty = 1$, the trapezoidal method is recovered with second order accuracy. As with the 1D case (Figure 7) it can be deduced that increasing $\bar{\rho}^h_\infty$ effectively reduces the magnitude of error for both methods.

4.2.2. Error convergence for Navier-Stokes problem

The L^2 norms of the velocity and pressure field errors are shown for the GM and AM projection methods when considering Navier-Stokes flow in Figure 14. It is evident that the convergence slopes closely reflect the observations made for the Stokes flow problem, hence the same accuracy is attained.

4.3. Flow around a cylinder

In this example, the well known benchmark problem of flow around a stationary circular cylinder is investigated. The geometry dimensions and boundary conditions for the problem are shown Figure 15. The vertical

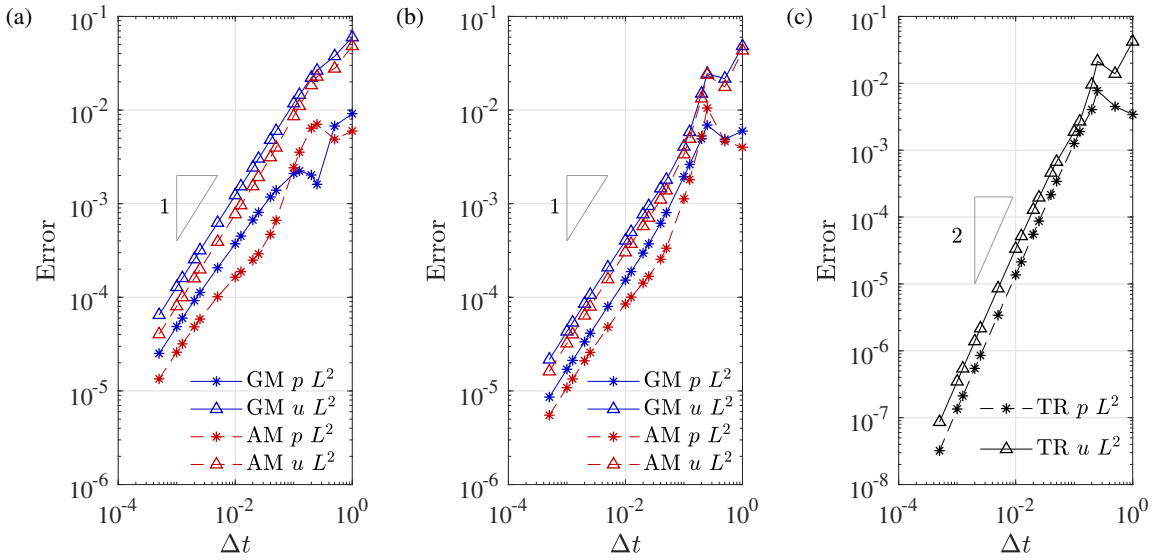

Figure 13: Stokes flow cavity model problem: Convergence rates for velocity and pressure field errors with (a) $\rho^h_\infty = 0$, (b) $\rho^h_\infty = 0.5$ and (c) $\rho^h_\infty = 1$.

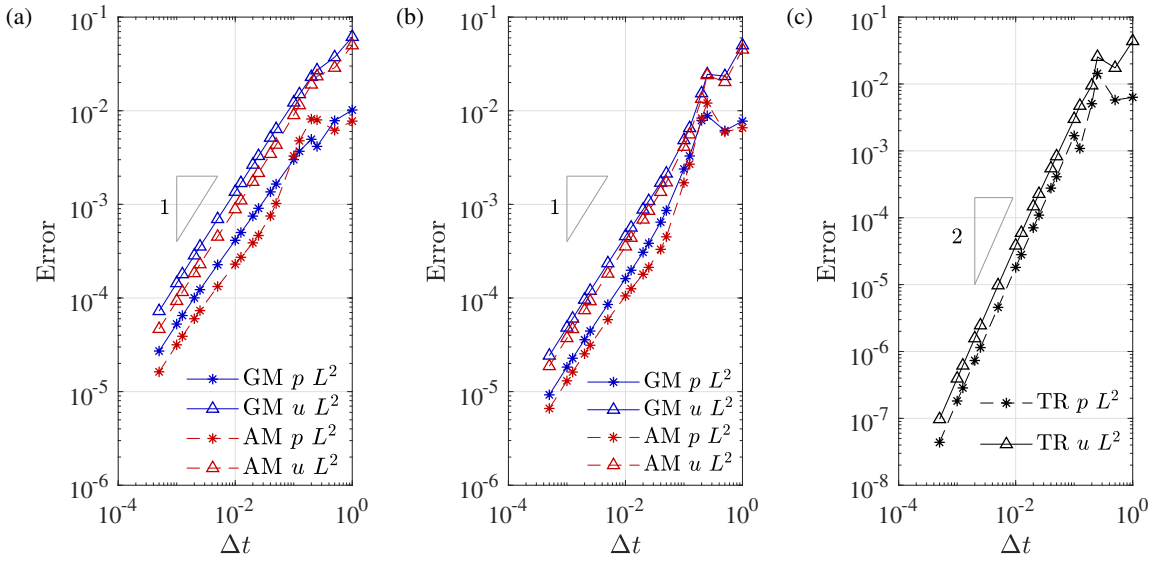

Figure 14: Navier-Stokes flow cavity model problem: Convergence rates for velocity and pressure field errors with (a) $\rho_\infty^h = 0$, (b) $\rho_\infty^h = 0.5$ and (c) $\rho_\infty^h = 1$.

velocity component v is prescribed as zero on the upper and lower boundaries, while the horizontal component u remains free. Also the pressure is prescribed as zero at the outlet boundary, and u is prescribed uniformly as u_∞ on the inlet boundary, in compliance with the assumption that the flow is uniform far away from the cylinder. In the analyses to follow, the parameters are set as $u_\infty = 1$, $\mu = 0.01$, $\rho = 1$ and $d = 1$, such that $Re = 100$. The mesh employed possesses 1708 elements (3472 P_2 nodes), as shown in Figure 15.

For the purpose of this study, several dimensionless quantities are defined. The coefficients of lift and drag,

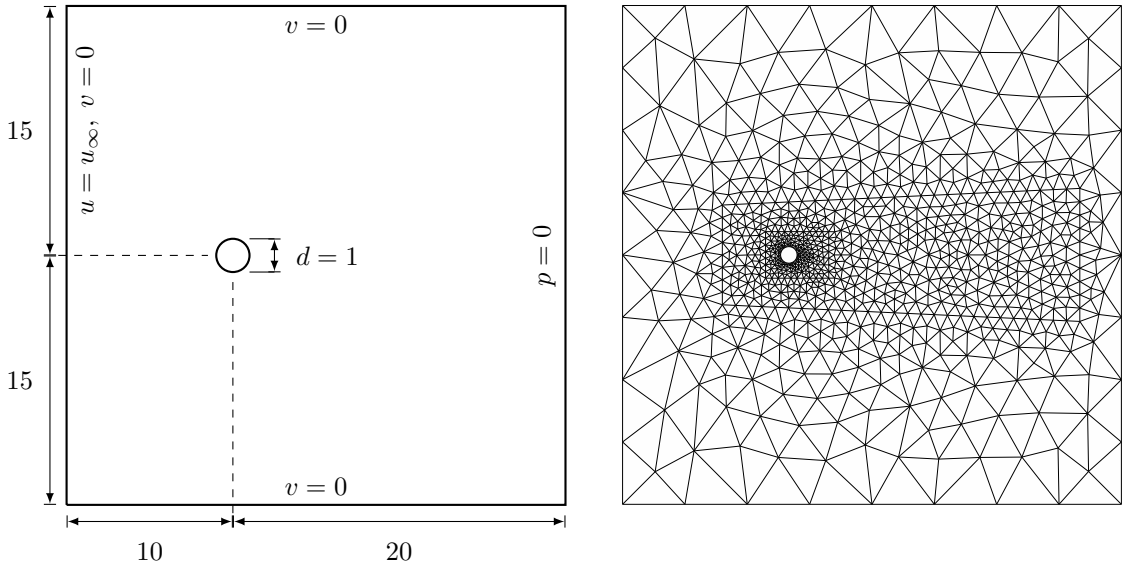

Figure 15: Flow around a cylinder: Geometry (not to scale), boundary conditions and mesh.

C_L and C_D, as well as the Strouhal number St are evaluated using the expressions

$$C_L(t) = \frac{F_L(t)}{\frac{1}{2}\rho u_\infty^2 d}, \quad C_D(t) = \frac{F_D(t)}{\frac{1}{2}\rho u_\infty^2 d}, \quad St = \frac{fd}{u_\infty} \tag{4.3}$$

where F_L and F_D are the lift and drag forces respectively, and f is the frequency of the lift force.

Figure 16 shows the C_L and C_D evolution with time for $Re = 100$. The C_L amplitude and St number are obtained as $C_L = \pm 0.292$ and $St = 0.165$ respectively, for a time step of $\Delta t = 0.01$. Due to the lack of analytical solutions, a comparison is made to experimental data by Roshko [47] and numerical data by Kadapa *et al.* [48]. The St number agrees well with the experimental data found in [47], where a best-fit line for experimentally obtained data is presented, i.e. $St = 0.212(1 - 21.2/Re)$, which yields $St = 0.167$ for $Re = 100$. An extensive numerical study carried out in [48], compares results obtained for C_L and St coefficients at $Re = 100$ by various authors. The C_L amplitudes range between ± 0.250 and ± 0.341, and St number, between 0.160 and 0.175. Clearly the results of the present study lie within this range.

The variation of the lift amplitude and the Strouhal number with the time step size is displayed in Figure 17. The convergence as $\Delta t \to 0$ is clearly visible. It can also be observed that the AM projection scheme performs significantly better than the respective GM scheme and that both schemes render more accurate results for $\bar{\rho}_\infty^h = 0.5$ than for $\bar{\rho}_\infty^h = 0$.

The temporal C_L amplitude and St errors are shown for the GM and AM projection methods with $\bar{\rho}_\infty^h$ set to 0 and 0.5 in Figure 18. The errors are computed by comparing the solutions to that of a reference solution obtained from a monolothic AM solver on the same spatial discretisation with $\bar{\rho}_\infty^h = 0.5$ and $\Delta t = 0.0005$. Thus, similar to Section 4.2, the term "error" refers to the deviation from the mesh-dependent limit solution, rather than from the exact solution. For the same mesh, the lift coefficients and the Strouhal numbers obtained from the monolithic solver, the GM and AM projection schemes all converge to the same values. The projections methods display first order accuracy, with the AM method achieving a lower magnitude of error than the GM method for the same respective values of $\bar{\rho}_\infty^h$.

Figure 19 similarly shows the C_L and St errors when considering the GM and AM projection methods with $\bar{\rho}_\infty^h = 0.9$. Observing the C_L convergence, it is visible that there is an increase of the slope at larger time steps for both methods. In comparison to Figure 18, a decrease in the magnitude of error is observed.

Figure 20 shows the convergence of the AM projection method for $\delta = 1$ and $\bar{\rho}_\infty^h = 0.9$ in comparison to its monolithic counterpart. It is evident that the solutions for C_L and St become unstable at around $\Delta t \approx 0.04$. This is attributed to the lack of numerical damping of the method, which has been demonstrated in Section 2.4.2.

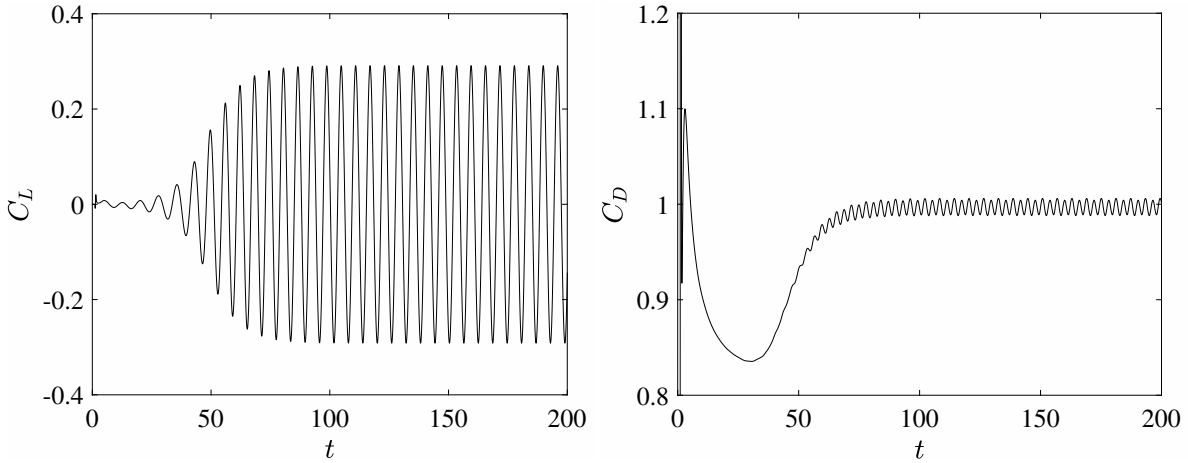

Figure 16: Flow around a cylinder: Evolution with time for the lift coefficient C_L (left), and drag coefficient C_D (right), considering the AM projection method with $\rho_\infty^h = 0.5$, $Re = 100$, $\Delta t = 0.01$, and 1708 elements.

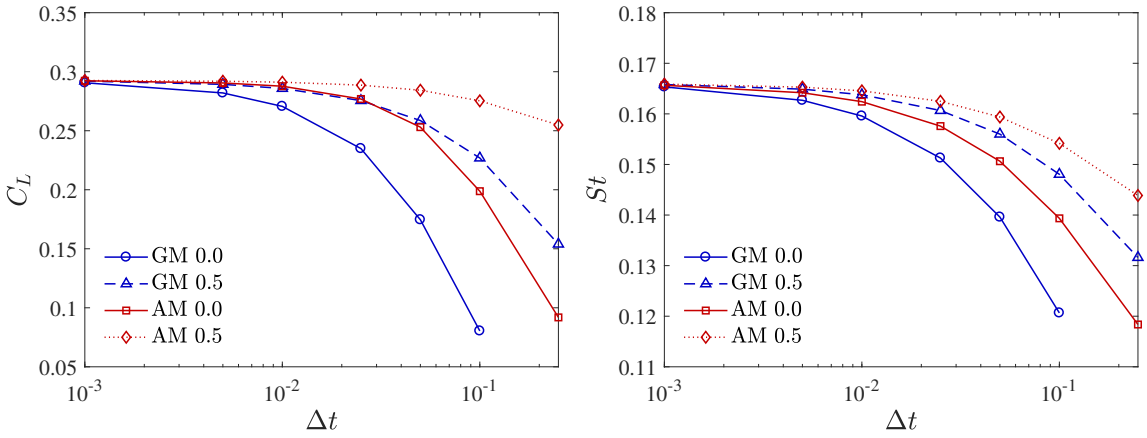

Figure 17: Flow around a cylinder: C_L amplitude convergence (left), and St convergence (right), for $Re = 100$.

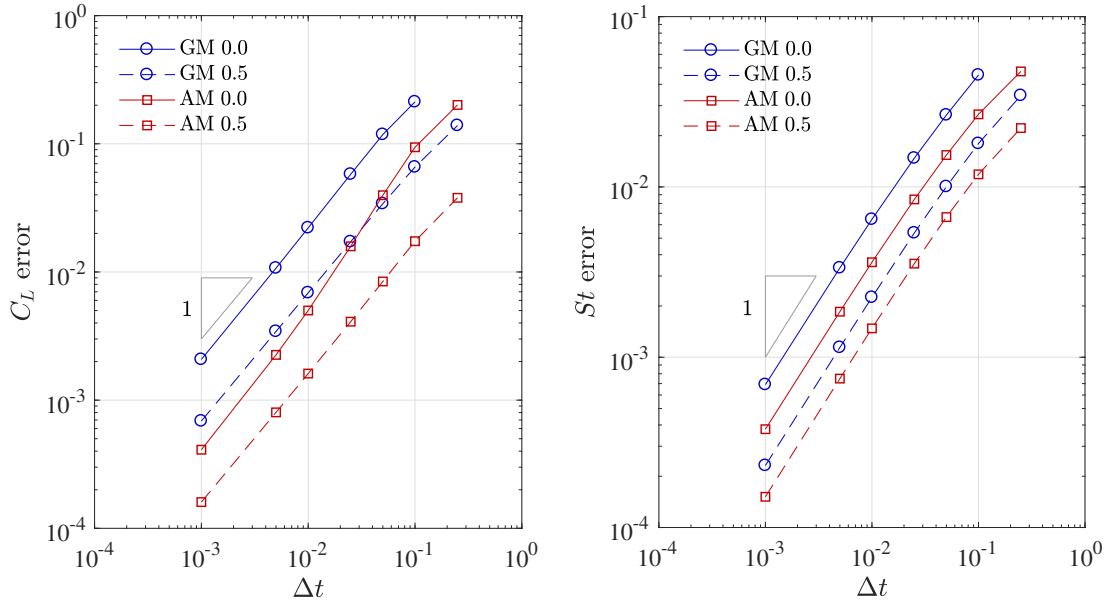

Figure 18: Flow around a cylinder: C_L amplitude error convergence (left), and St error convergence (right), for GM and AM projection methods with $\bar{\rho}^h_\infty$ set to 0 and 0.5.

Summarising, the performance of the GM and AM strategies for the flow around the cylinder are consistent with the analyis of the model problem in Section 2.

5. Conclusions

In Section 2 a discrete model problem consisting of point masses and dash-pots has been introduced, which allows for insight into the performance of projection schemes, including aspects which are otherwise difficult to assess, in particular the numerical damping. The investigation performed in Section 2, on the basis of this model problem, suggests that a second order accurate projection scheme cannot possess any high frequency damping.

Also in Section 2, two new methodologies have been proposed which may offer a compromise between accuracy and high-frequency damping. In particular it has been investigated to what extent the properties of the generalised-α method can be maintained when moving from a monolithic scheme to a projection scheme.

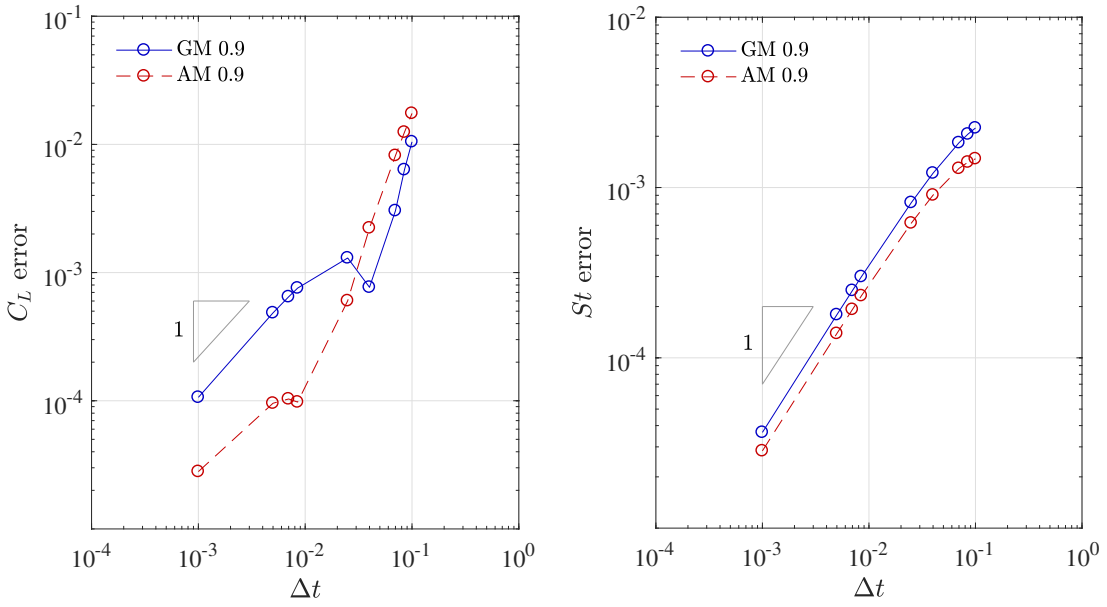

Figure 19: Flow around a cylinder: C_L amplitude error convergence (left), and St error convergence (right), with $\bar{\rho}_\infty^h = 0.9$ for the GM and AM methods

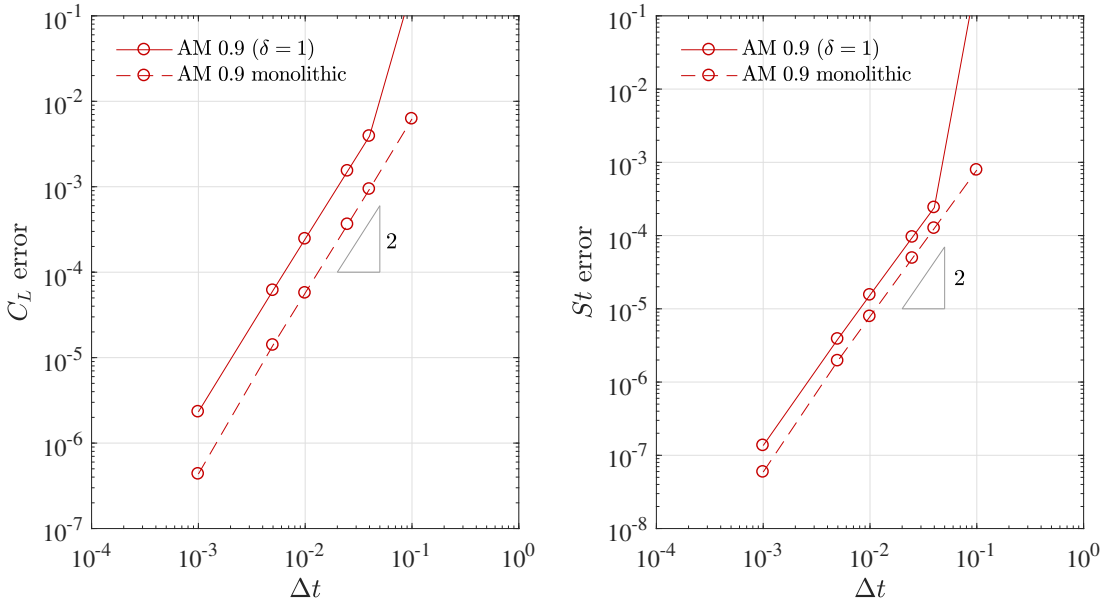

Figure 20: Flow around a cylinder: C_L amplitude error convergence (left), and St error convergence (right), with $\bar{\rho}_\infty^h = 0.9$ for the GM and AM methods.

In Section 3 the proposed methodologies have been applied to the incompressible Navier-Stokes equations and it has been shown that the additional computational cost of the AM projection scheme is negligible in comparison to the proposed GM or standard BE projection schemes.

Numerical examples based on the lid-driven cavity and the flow around a cylinder have been presented in Section 4. The results obtained are consistent with the conclusions drawn from the model problem and thus confirm its suitability and relevance for studying different types of projection schemes. For the same spatial discretisation, the GM and AM projection schemes and the fully implicit monolithic solver converge to the same

response as the time step size is reduced. The study of the flow around the cylinder includes the presentation of convergence diagrams for the lift coefficient and the Strouhal number which, to the best of our knowledge, have not been shown elsewhere in the context of projection schemes.

For the model problem and for the Navier-Stokes equations, the proposed AM projection scheme consistently outperforms the associated GM projection scheme with the same amount of high-frequency damping by a notable margin (see most notably Figures 2 and 17). The comparison of the more accurate AM projection scheme to the widely used standard first order schemes based on BE time integration is very favourable.

6. References

[1] A. J. Chorin. A numerical method for solving incompressible viscous flow problems. *Journal of Computational Physics*, 2(1):12–26, 1967.

[2] R. Temam. *Navier-Stokes Equations: Theory and numerical analysis*. North-Holland Publishing Company, New York, 1977.

[3] K. Goda. A multistep technique with implicit difference schemes for calculating two- or three-dimensional cavity flows. *Journal of Computational Physics*, 30:76–95, 1979.

[4] J. van Kan. A second-order accurate pressure-correction scheme for viscous incompressible flow. *SIAM Journal on Scientific and Statistical Computing*, 7(3):870–891, 1986.

[5] J. L. Guermond and J. Shen. Velocity-correction projection methods for incompressible flows. *SIAM Journal on Numerical Analysis*, 41(1):112–134, 2003.

[6] J. L. Guermond and J. Shen. A new class of truly consistent splitting schemes for incompressible flows. *Journal of Computational Physics*, 192:262–276, 2003.

[7] J. Blasco, R. Codina, and A. Huerta. A fractional-step method for the incompressible Navier-Stokes equations related to a predictor-multicorrector algorithm. *International Journal for Numerical Methods in Fluids*, 28:1391–1419, 1998.

[8] P. Nithiarasu, R. Codina, and O. C. Zienkiewicz. The characteristic-based split (CBS) scheme - a unified approach to fluid dynamics. *International Journal for Numerical Methods in Engineering*, 66:1514–1546, 2006.

[9] R. Temam. *Navier-Stokes equations and nonlinear functional analysis*. Society for Industrial and Applied Mathematics, 1995.

[10] S. Badia and R. Codina. Algebraic pressure segregation methods for the incompressible Navier-Stokes equations. *Archives of Computational Methods in Engineering*, 15:343 – 369, 2008.

[11] J. L. Guermond, P. Minev, and J. Shen. An overview of projection methods for incompressible flows. *Computer Methods in Applied Mechanics and Engineering*, 195:6011–6045, 1998.

[12] R. Bevan, E. Boileau, R. van Loon, R. W. Lewis, and P. Nithiarasu. A comparative study of fractional step method in its quasi-implicit, semi-implicit and fully-explicit forms for incompressible flows. *International Journal of Numerical Methods for Heat & Fluid Flow*, 26(3/4):595–623, 2016.

[13] J. H. Pyo and J. Shen. Normal mode analysis of second-order projection methods for incompressible flows. *Discrete and continuous dynamical systems-series B*, 5(3):817–840, 2005.

[14] K. E. Jansen, C. H. Whiting, and G. M. Hulbert. A generalized-α method for integrating the filtered Navier-Stokes equations with a stabilized finite element method. *Computer Methods in Applied Mechanics and Engineering*, 190:305–319, 2000.

[15] W. G. Dettmer and D. Perić. A new staggered scheme for fluid-structure interaction. *International Journal for Numerical Methods in Engineering*, 93:1–22, 2013.

[16] M. M. Joosten, W. G. Dettmer, and D. Perić. On the temporal stability and accuracy of coupled problems with reference to fluid-structure interaction. *International Journal for Numerical Methods in Fluids*, 64:1363–1378, 2010.

[17] M. M. Joosten, W. G. Dettmer, and D. Perić. Analysis of the block Gauss-Seidel solution procedure for a strongly coupled model problem with reference to fluid-structure interaction. *International Journal for Numerical Methods in Engineering*, 78:757–778, 2009.

[18] A. Mini, C. Lerch, R. Wüchner, and K. Bletzinger. Computational closed-loop control of fluid-structure interaction (FSCI) for lightweight structures. *PAMM Proceedings in Applied Mathematics and Mechanics*, 16:15–18, 2016.

[19] X. Chen, M. Schäfer, and D. Bothe. Numerical modeling and investigation of viscoelastic fluid-structure interaction applying an implicit partitioned coupling algorithm. *Journal of Fluids and Structures*, 54:390–421, 2015.

[20] C. Kadapa, W. G. Dettmer, and D. Perić. A stabilised immersed boundary method on hierarchical b-spline grids for fluid-rigid body interaction with solid-solid contact. *Computer Methods in Applied Mechanics and Engineering*, 318:242–269, 2015.

[21] W. G. Dettmer and D. Perić. A computational framework for fluid-structure interaction: Finite element formulation and applications. *Computer Methods in Applied Mechanics and Engineering*, 195:5754–5779, 2006.

[22] W. G. Dettmer and D. Perić. An analysis of the time integration algorithms for the finite element solutions of incompressible Navier-Stokes equations based on a stabilised formulation. *Computer Methods in Applied Mechanics and Engineering*, 192:1177–1226, 2003.

[23] Y. Bazilevs, K. Takizawa, and T. E. Tezduyar. *Computational Fluid-Structure Interaction: Methods and Applications*. John Wiley & Sons, Inc., 2013.

[24] J. Chung and G. M. Hulbert. A time integration algorithm for structural dynamics with improved numerical dissipation: The generalized-α method. *Journal of Applied Mechanics*, 60:371–375, 1993.

[25] C. Kadapa, W. G. Dettmer, and D. Perić. On the advantages of using the first-order generalised-alpha scheme for structural dynamic problems. *Computers & Structures*, 193:226–238, 2017.

[26] L. J. P. Timmermans, P. D. Minev, and F. N. Van De Vosse. An approximate projection scheme for incompressible flow using spectral elements. *International Journal for Numerical Methods in Fluids*, 22:673–688, 1996.

[27] J Kim and P Moin. Application of a fractional-step method to incompressible Navier-Stokes equations. *Journal of Computational Physics*, 59(2):308 – 323, 1985.

[28] T. Rüberg and F. Cirak. A fixed-grid b-spline finite element technique for fluid-structure interaction. *International Journal for Numerical Methods in Fluids*, 75(9):623–660, 2013.

[29] J. C. Pedro, M. K. Banda, and P. Sibanda. Implicit-explicit higher-order time integration schemes for computations of structural dynamics with fluid-structure interaction. *Applications and Applied Mathematics: An International Journal*, 10:287–311, 2015.

[30] W. G. Dettmer. *Finite Element Modelling of Fluid Flow with Moving Free Surfaces and Interfaces Including Fluid-Solid Interaction*. Phd thesis, Swansea University, 2004.

[31] X. Zeng, G. Scovazzi, N Abboud, O. Colomés, and S. Rossi. A dynamic variational multiscale method for viscoelasticity using linear tetrahedral elements. *International Journal for Numerical Methods in Engineering*, xxx:xxx–xxx, DOI: 10.1002/nme.5591.

[32] J. L. Guermond and L. Quartapelle. Calculation of incompressible viscous flows by an unconditionally stable projection FEM. *Journal of Computational Physics*, 132:12–33, 1997.

[33] J. L. Guermond and L. Quartapelle. On incremental projection methods. *R. Salvi (Ed.), Pitman, Research Notes in Mathematics Series*, 388:277–288, 1998.

[34] I. Babuška. Error-bounds for finite element method. *Numerische Mathematik*, 16:322–333, 1971.

[35] F. Brezzi. On the existence, uniqueness and approximation of saddle-point problems arising from lagrangian multipliers. *ESAIM: Mathematical Modelling and Numerical Analysis*, 8:129–151, 1974.

[36] F. Brezzi and J. Douglas Jr. Stabilized mixed methods for the Stokes problem. *Numerische Mathematik*, 53:225–235, 1988.

[37] F. Brezzi and M. Fortin. *Mixed and Hybrid Finite Element Methods*. Springer-Verlag, 1991.

[38] F. Brezzi and R. S. Falk. Stability of higher-order Hood-Taylor methods. *SIAM Journal on Numerical Analysis*, 28:581–590, 1991.

[39] A. N. Brooks and T. J. R. Hughes. Streamline upwind/Petrov-Galerkin formulations for convection dominated flows with particular emphasis on the incompressible Navier-Stokes equations. *Computer Methods in Applied Mechanics and Engineering*, 32:199–259, 1982.

[40] T. E. Tezduyar. Stabilized finite element formulations for incompressible flow computations. *Advances in Applied Mechanics*, 28:1–44, 1991.

[41] T. E. Tezduyar, S. Mittal, S. E. Ray, and R. Shih. Incompressible flow computations with stabilized bilinear and linear equal-order-interpolation velocity-pressure elements. *Computer Methods in Applied Mechanics and Engineering*, 95:221–242, 1992.

[42] T. Tezduyar. Stabilization parameters in SUPG and PSPG formulations. *Journal of Computational and Applied Mechanics*, 4(1):71–88, 2003.

[43] G. Lube. Stabilized FEM for incompressible flow: A critical review and new trends. In *European Conference on Computational Fluid Dynamics ECCOMAS CFD 2006*, 2006.

[44] T. J. R. Hughes, G. Scovazzi, and L. P. Franca. *Multiscale and Stabilized Methods, Encyclopedia of Computational Mechanics*. Wiley, 2004.

[45] J. L. Guermond and L. Quartapelle. On stability and convergence of projection methods based on pressure Poisson equation. *International Journal for Numerical Methods in Fluids*, 26:1039–1053, 1998.

[46] W. G. Dettmer, C. Kadapa, and D. Perić. A stabilised immersed boundary method on hierarchical b-spline grids. *Computer Methods in Applied Mechanics and Engineering*, 311:415–437, 2016.

[47] A. Roshko. On the development of turbulent wakes from vortex streets. National advisory committe for aeronautics, California Institute of Technology, 1954.

[48] C. Kadapa, W. G. Dettmer, and D. Perić. A fictitious domain/distributed Lagrange multiplier based fluid-structure interaction scheme with hierarchical b-spline grids. *Computer Methods in Applied Mechanics and Engineering*, 301:1–27, 2015.